CrossMark

The IGRINS YSO Survey. I. Stellar Parameters of Pre-main-sequence Stars in Taurus-Auriga

Ricardo López-Valdivia[1] , Kimberly R. Sokal[1] , Gregory N. Mace[1] , Benjamin T. Kidder[1] , Maryam Hussaini[1] ,
Larissa Nofi[2,3] , L. Prato[2] , Christopher M. Johns-Krull[4] , Heeyoung Oh[1,5] , Jae-Joon Lee[5] , Chan Park[5] , Jae Sok Oh[5],
Adam Kraus[1] , Kyle F. Kaplan[6] , Joe Llama[2] , Andrew W. Mann[7] , Hwihyun Kim[8] , Michael A. Gully-Santiago[1] ,
Hye-In Lee[5], Soojong Pak[9] , Narae Hwang[5] , and Daniel T. Jaffe[1]

[1] The University of Texas at Austin, Department of Astronomy, 2515 Speedway, Stop C1400, Austin, TX 78712-1205, USA; rlopezv@utexas.edu
[2] Lowell Observatory, 1400 W. Mars Hill Rd, Flagstaff, AZ 86001, USA
[3] Institute for Astronomy, University of Hawaii Manoa, 2680 Woodlawn Drive, Honolulu, HI 96822, USA
[4] Physics & Astronomy Dept., Rice University, 6100 Main St., Houston, TX 77005, USA
[5] Korea Astronomy and Space Science Institute, 776 Daedeok-daero, Yuseong-gu, Daejeon 34055, Republic of Korea
[6] SOFIA Science Center—USRA, NASA Ames Research Center, Moffett Field, CA 94035, USA
[7] Department of Physics and Astronomy, University of North Carolina at Chapel Hill, Chapel Hill, NC 27599, USA
[8] Gemini Observatory/NSF's NOIRLab, Casilla 603, La Serena, Chile
[9] School of Space Research, Kyung Hee University, 1732 Deogyeong-daero, Giheung-gu, Yongin-si,Gyeonggi-do 17104, Republic of Korea

Abstract

We present fundamental parameters for 110 canonical K- and M-type ($1.3-0.13\,M_\odot$) Taurus-Auriga young stellar objects (YSOs). The analysis produces a simultaneous determination of effective temperature (T_{eff}), surface gravity (log g), magnetic-field strength (B), and projected rotational velocity ($v \sin i$). Our method employed synthetic spectra and high-resolution ($R \sim 45{,}000$) near-infrared spectra taken with the Immersion GRating INfrared Spectrometer (IGRINS) to fit specific K-band spectral regions most sensitive to those parameters. The use of these high-resolution spectra reduces the influence of distance uncertainties, reddening, and non-photospheric continuum emission on the parameter determinations. The median total (fit + systematic) uncertainties were 170 K, 0.28 dex, 0.60 kG, 2.5 km s^{-1} for T_{eff}, log g, B, and $v \sin i$, respectively. We determined B for 41 Taurus YSOs (upper limits for the remainder) and find systematic offsets (lower T_{eff}, higher log g and $v \sin i$) in parameters when B is measurable but not considered in the fit. The average log g for the Class II and Class III objects differs by 0.23 ± 0.05 dex, which is consistent with Class III objects being the more evolved members of the star-forming region. However, the dispersion in log g is greater than the uncertainties, which highlights how the YSO classification correlates with age (log g), yet there are exceptionally young (lower log g) Class III YSOs and relatively old (higher log g) Class II YSOs with unexplained evolutionary histories. The spectra from this work are provided in an online repository along with TW Hydrae Association comparison objects and the model grid used in our analysis.

Supporting material: machine-readable table

1. Introduction

Young stellar objects (YSOs) are stars at an early stage of evolution, and the disks surrounding them provide the raw material out of which planets can form. An empirically determined lifetime for protoplanetary disks is key to differentiating theories of planet formation and migration (e.g., Baruteau et al. 2014). At a population level, observations of disk fractions in star-forming regions and moving groups, with ages determined by comparing stellar properties to theoretical isochrones, have established a characteristic time-scale of 2–3 Myr for YSO disk dissipation (e.g., Haisch et al. 2001; Hernández et al. 2007; Mamajek 2009; Ribas et al. 2014). These studies also make it clear that there is heterogeneity in the YSO population, with very young clusters having diskless members and a small number of systems with thick disks remaining at 8–10 Myr (e.g., TW Hydra, Sokal et al. 2018, and references therein). There are some indications of differences as a function of mass (Galli et al. 2015; Ribas et al. 2015), but mass-dependence does not explain many of the exceptional cases.

The combination of ALMA imaging of the outer disks of YSOs (e.g., ALMA Partnership et al. 2015; Barenfeld et al. 2017; Huang et al. 2018; Long et al. 2019; Pérez et al. 2020) and infrared interferometry and spectroscopy of inner disks (e.g., Muzerolle et al. 2003; Varga et al. 2017; Boccaletti et al. 2020) is providing new details on disk structure, kinematics, and composition. Both the puzzle of lifetime variation and new details about the disks themselves drive a need for more precise information about the stellar hosts. Effective temperature (T_{eff}) and surface gravity (log g), as proxies for YSO masses and ages, respectively (see Figure 9 of Sokal et al. 2018), permit comparisons of disk classifications with evolutionary models (Baraffe et al. 2015; Simon et al. 2019). Since angular momentum transport is very important both to the disks and to the evolution of stellar rotation (e.g., Attridge & Herbst 1992; Herbst et al. 2007; Bouvier et al. 2014), measures of the rotation are also needed. Magnetic interactions between a star and disk are crucial for accretion onto the star and material flow through the disk (e.g., Camenzind 1990; Koenigl 1991; López-

Santiago et al. 2016). We therefore also need estimates of stellar magnetic-field strength.

However, measurements of YSO parameters are influenced by interstellar reddening, continuum veiling, and stellar spots. The impacts of interstellar reddening are reduced at longer wavelengths, making the infrared more amenable to YSO studies than visible-light observations. The presence of strong magnetic fields (B) is associated with cool spots (e.g., Crockett et al. 2012; Gully-Santiago et al. 2017), Zeeman-split atomic spectral lines (e.g., Johns-Krull et al. 1999; Doppmann et al. 2003; Yang et al. 2005; Yang & Johns-Krull 2011; Lavail et al. 2017; Sokal et al. 2018; Lavail et al. 2019; Sokal et al. 2020), and changes in absorption-line profiles. Veiling (r) is a non-stellar continuum emission that reduces the depth of the photospheric lines in YSO spectra (Joy 1949). It has been explained as the consequence of different physical processes including an active chromosphere (e.g., Calvet et al. 1984; Basri & Bertout 1989; Hartigan et al. 1989; Hartmann & Kenyon 1990; Valenti et al. 1993; Cieza et al. 2005), emission produced by accretion onto the star (e.g., Kenyon & Hartmann 1987; Johns-Krull & Valenti 2001; Gahm et al. 2008), excess emission from dust at the sublimation radius of the inner disk wall (e.g., Natta et al. 2001; Muzerolle et al. 2003), and emission from warm gas located inside the dust sublimation radius of the disk (e.g., Fischer et al. 2011). These variable processes can result in YSO parameters that differ significantly between literature references because the YSOs were observed at different times, in different physical states, and with instruments observing different wavelengths.

We have employed the Immersion GRating INfrared Spectrometer (IGRINS; Yuk et al. 2010; Park et al. 2014; Mace et al. 2016) to survey the Taurus-Auriga star-forming region and determine YSO properties while minimizing the effects listed above. With its broad spectral grasp (1.45–2.5 μm) at high resolution ($R \sim 45,000$), IGRINS simultaneously observes numerous spectral features of YSOs. Additionally, we can average over variability and derive typical parameters for each target by combining multiple observation epochs. In 2014, IGRINS was commissioned on the 2.7 m Harlan J. Smith Telescope at McDonald Observatory. Observations initially focused on the Taurus-Auriga complex (often recognized as Taurus) because it is a close ($d = 140$ pc, Kenyon et al. 1994; Galli et al. 2018) and young (about 1–5 Myr, Kraus & Hillenbrand 2009; Gennaro et al. 2012) star-forming region that provides observations of YSOs at various stages of evolution. The population of Taurus is at an age coincident with disk dissipation timescales and includes both Class II and Class III YSOs.

The IGRINS YSO Survey is uniquely suited to the determination of physical parameters because:

1. The 1.45–2.5 μm spectral region includes both photospheric and disk contributions to the YSO spectrum.
2. The fixed spectral format of IGRINS provides similar spectral products for each object at each epoch.
3. Multiple-epoch observations provide a means to characterize and average over variability.
4. The spectral resolution of $\sim$7 km s^{-1} is smaller than the typical rotational velocity of young stars and can reliably resolve line splitting by magnetic fields (B) $\gtrsim 1.0$ kG.

In this paper, we present the simultaneous determination of $T_{\rm eff}$, log g, B, and projected rotational velocity ($v \sin i$) of 119

K- & M-type YSOs located in Taurus, of which 110 are reliable. In Section 2 we describe the sample and the IGRINS observations. Section 3 details the parameter determination and sources of uncertainty, while in Section 4 we discuss the results and provide analysis. In Section 5 we provide a summary and the conclusions of this work.

2. Observations and Sample

IGRINS employs a silicon immersion grating as the primary disperser (Jaffe et al. 1998; Wang et al. 2010; Gully-Santiago et al. 2010) and volume-phase holographic gratings to cross disperse the H- and K-band echellograms onto Teledyne Hawaii-2RG arrays. This setup provides a compact design with high sensitivity and a significant single-exposure spectral grasp (Yuk et al. 2010; Park et al. 2014). IGRINS has a fixed spectral format and no moving optics, so the science products remain unchanged no matter where it is installed. IGRINS has increased its scientific value by traveling between McDonald Observatory, the Lowell Discovery Telescope (LDT), and the Gemini South telescope (Mace et al. 2018).

Flat-field calibration frames were taken at the start of each night and used for bad-pixel masking and 2D aperture definitions. All the YSOs in our sample were observed by nodding the targets along the slit in patterns made up of AB or BA pairs. An A0V telluric standard star was observed at a similar airmass within a period of two hours before or after the science target. Flexure between the target and A0V observations was sub-pixel (Mace et al. 2016). The airmass during the IGRINS observations ranged from 1.00 to 2.17. We used the IGRINS exposure time calculator[10] to estimate the exposure time of each object. The total exposure time varied from minutes to hours to achieve a signal-to-noise ratio (SNR) > 100.

All IGRINS data were reduced using the IGRINS pipeline (Lee et al. 2017)[11] which produces a telluric-corrected spectrum with a wavelength solution derived from OH night-sky emission lines at shorter wavelengths and telluric absorption lines at wavelengths greater than 2.2 μm. Telluric correction was performed by dividing the target spectrum by an A0V spectral standard and multiplying by a standard Vega model. We corrected for any sub-pixel shifts between the target and A0V observations (due to instrument flexure) by aligning the spectra at a strong telluric absorption feature. Finally, the wavelength solution of the target was corrected for the barycenter velocity derived using ZBARYCORR (Wright & Eastman 2014) along with the Julian date at the midpoint of observation and the telescope site. The telluric correction uncertainties were propagated into the telluric-corrected spectra by combining the observed uncertainties of the target and standard spectra in quadrature.

To construct the YSO sample used in this work, we looked into the reduced science spectral archive of IGRINS for targets classified as Taurus members by Luhman et al. (2010), with a spectral type (SpT) between K0 and M5 (Luhman et al. 2017), and a minimum average SNR of 50 in the K-band. The latter condition resulted in more than 500 single-visit observations of 139 Taurus YSOs observed with IGRINS on the McDonald 2.7 m telescope and LDT between 2014 and 2017. This sample

---

contains many of the canonical Taurus-Auriga members with K-band magnitudes <10 mag and according to the classifications made by Kenyon & Hartmann (1995), Luhman et al. (2010), Rebull et al. (2010), Esplin et al. (2014), and Kraus et al. (2017), there are 9 Class I, 91 Class II, and 39 Class III YSOs. Finally, we visually checked the K-band spectrum of these 139 YSOs, and we excluded objects with shallow ($<2\%$) lines due to high veiling or $v \sin i$ values. After this cleaning step, our final sample (see Table 1) contained 119 YSOs (84 Class II and 35 Class III). Figure 1 depicts the spectral type (Luhman et al. 2017), 2MASS K-band magnitude (Cutri et al. 2003) and the number-of-epoch distributions of the 119 YSOs that define our sample.

By compiling the survey sample from the IGRINS spectral archive, we identify some biases in the sample selection. First, for the same effective temperature ($T_{\rm eff} \lesssim 4000$ K), younger stars are brighter because of their larger radii (Hayashi 1961). These young and bright stars were easier to observe at high spectral resolution. The full census of Taurus YSOs is >400 members (Luhman 2018). Our survey includes only $\sim 45\%$ (116 out of 258) of the Taurus YSOs between spectral types K0 and M5 since we have not observed the faintest or more widely distributed members (Kraus et al. 2017). Lastly, binary stars are the specific focus of some IGRINS YSO observing programs. The combined flux of the two binary components makes them brighter, which results in higher SNRs, but their analysis is also complicated by line blending in the composite spectrum. In this work we have identified known binaries (or multiples) in the literature and have compared the single and multiple samples. A more rigorous identification, analysis, and characterization of binarity will be the topic of a future study.

The final combined spectrum of each target was made up of between 1 and 10 epochs, with a median value of 4 epochs. If more than 10 epochs were available, we chose the best 10 based on a combination of airmass, SNR, and the quality of the telluric correction. We shifted each epoch to the wavelength rest frame by determining the radial velocity shift of Na lines at 2.206 and 2.209 μm. Then, we produced the combined spectrum by taking a weighted average of all epochs where the weight corresponded to the SNR at each data point. The standard deviation of the mean gave the final uncertainties per data point.

In 2018, we observed members of the TW Hydrae Association (TWA; Kastner et al. 1997) while IGRINS visited the 8.1 m Gemini South telescope (Mace et al. 2018). We reduced the TWA objects in the same fashion as the Taurus sample, but all TWA observations were single-epoch and final combined spectra were not produced. The collection of IGRINS spectra is available from the Harvard Dataverse (López-Valdivia 2021a, 2021b)[12].

3. Stellar Parameter Determination

To determine $T_{\rm eff}$, log g, B, and $v \sin i$ we used a Markov Chain Monte Carlo (MCMC) algorithm comparing observations with synthetic spectra, which we describe here in detail.

3.1. Theoretical Grid

We computed a four-dimensional ($T_{\rm eff}$, log g, B, $v \sin i$) grid of synthetic spectra using the MOOGSTOKES code (Deen 2013).

MOOGSTOKES is a customization of the one-dimensional LTE radiative transfer code MOOG (Sneden 1973) that synthesizes the emergent spectrum of a star taking into account the Zeeman splitting produced by the presence of a photospheric magnetic field. It assumes a uniform and purely radial magnetic field and uniform $T_{\rm eff}$ and log g, producing a disk-averaged spectrum broadened to the user-specified spectral resolution and $v \sin i$ values.

To synthesize a spectrum with MOOGSTOKES, the program required a model atmosphere and an atomic/molecular line list. The $T_{\rm eff}$, log g, and metallicity of the resulting spectrum are defined by the model atmosphere, while B, $v \sin i$, and spectral resolution are user-selected quantities. In this work, we used the MARCS atmospheric models (Gustafsson et al. 2008) with solar metallicity (suitable for YSOs; Padgett 1996; Santos et al. 2008; D'Orazi et al. 2011) and the Vienna Atomic Line Database (VALD3; Ryabchikova et al. 2015). Often, the atomic data coming from databases are not accurate enough to reproduce the solar spectrum at high resolution, requiring modifications to some of the absorption-line oscillator strengths and van der Wals constants. In this work we used the astrophysical-inferred modifications to the VALD atomic data presented by Flores et al. (2019). Low-mass stars have microturbulence values between 0 and 2 km s^{-1} (e.g., Gray 2005; Reid & Hawley 2005; Bean et al. 2006), thus for this study we used a microturbulence of 1 km s^{-1}. Finally, we selected B values up to 4 kG, $v \sin i$ between 2 and 50 km s^{-1}, and matched the IGRINS spectral resolution ($R \sim 45{,}000$).

Our grid of synthetic spectra covers the parameter space as follows: from 3000 to 5000 K in $T_{\rm eff}$ (steps of 100 K up to 4000 K, and 250 K above 4000 K), from 3.0 to 5.0 dex in log g (steps of 0.5 dex), from 0 to 4 kG in B (steps of 0.5 kG), and values from 2 to 50 km s^{-1} in $v \sin i$ (steps of 2 km s^{-1}). The grid steps[13] are well suited to our study as they are enough to see the effects of these parameters on the spectra. Smaller step sizes in the model grid would drastically increase the computation time without significantly altering the synthetic spectra. Instead, the grid was linearly interpolated at values between grid points. The grid of synthetic spectra does not cover the entire IGRINS spectrum, but only the spectral regions described in Section 3.2. The grid of synthetic spectra is also available from Harvard Dataverse (López-Valdivia 2021c).

3.2. Spectral Regions

We employed four spectral regions in the K band to determine the stellar parameters in this work. These regions are in four different K-band IGRINS orders. Each region is sensitive to changes in different stellar parameters, as shown by their use previously in K and M stars (e.g., Rajpurohit et al. 2018; Sokal et al. 2018; Flores et al. 2019).

Sokal et al. (2018) used three spectral intervals in the K band around Na ($\sim 2.210 \mu$m), Ti ($\sim 2.222 \mu$m), and CO ($\sim 2.295 \mu$m) features to determine $T_{\rm eff}$, log g, and B of the star TW Hydra. Recently, Flores et al. (2019) included the Ca I lines around 2.264 μm in the determination of the stellar parameters of the young stars BP Tau and V347 Aur with iSHELL (Rayner et al. 2016) infrared spectra at a similar spectral resolution to IGRINS.

---

13 The grid steps of $T_{\rm eff}$ and log g are defined by the model atmosphere, while we selected the steps of B and $v \sin i$.

Table 1
Compiled Information for the 119 Stars in Our Taurus YSO Sample, Including $T_{\rm eff}$, log g, B, and $v \sin i$

2MASS ID	Alt. Name	K (mag)	SpT	Class	Ref	Binary	Ref	N	SNR$_{\rm K}$	flag	$T_{\rm eff}$ (K)	log g (dex)	B (kG)	$v \sin i$ (km s^{-1})	$r_{\rm K}$
J04141760+2806096	[BCG93] 1	9.9	M5.0	II	1, 2, 3, 4	?	⋯	2	172	0	3281 ± 197	3.88 ± 0.40	<1.09	9.9 ± 2.9	1.10 ± 0.21
J05075496+2500156	[BCG93] 12	10.4	M3.7	II	2, 4	N	16	2	64	3	⋯	⋯	⋯	⋯	⋯
J04182909+2826191	[SS94] V410 Anon 25	9.9	M3.5	III	2, 4, 5	?	⋯	1	87	1	3619 ± 328	4.05 ± 0.59	<2.32	30.7 ± 7.4	0.39 ± 0.20
J04174965+2829362	[SS94] V410 X-ray 1	9.1	M3.7	II	2, 3, 4	N	16	2	182	0	3315 ± 129	3.37 ± 0.25	1.22 ± 0.33	9.7 ± 2.0	0.28 ± 0.06
J04183444+2830302	[SS94] V410 X-ray 2	9.2	M0.0	II	2, 4	?	⋯	2	182	0	4231 ± 143	4.53 ± 0.27	1.84 ± 0.49	10.9 ± 2.9	0.44 ± 0.08
J04345542+2428531	AA Tau	8.0	M0.6	II	1, 2, 3, 4	N	16	10	356	0	3751 ± 171	3.87 ± 0.26	2.16 ± 0.41	12.5 ± 2.3	1.56 ± 0.12
J04191583+2906269	BP Tau	7.7	M0.5	II	1, 2, 3, 4	N	16	7	353	0	3719 ± 131	4.01 ± 0.25	2.19 ± 0.37	9.9 ± 2.3	1.36 ± 0.11
J04335200+2250301	CI Tau	7.8	K5.5	II	2, 3, 4	N	16	10	931	0	3951 ± 94	3.77 ± 0.17	1.95 ± 0.31	12.5 ± 1.9	2.34 ± 0.09
J04265440+2606510	CoKu FV Tau c	8.9	M2.5	II	1, 2, 3, 4	Y	24	6	302	0	3456 ± 136	3.53 ± 0.23	<2.01	38.6 ± 2.4	0.33 ± 0.06
J04355349+2254089	CoKu HP Tau G3	8.8	M0.6	III	1, 2, 3, 4, 5	Y	16	6	239	0	3760 ± 164	3.84 ± 0.26	<2.65	43.3 ± 2.9	0.25 ± 0.07
J04354093+2411087	CoKu Tau 3	8.4	M0.5	II	1, 2, 3, 4	N	16	5	249	0	3665 ± 154	3.85 ± 0.26	2.33 ± 0.34	8.2 ± 2.1	0.77 ± 0.08
J04411681+2840000	CoKu Tau 4	8.7	M1.1	II	1, 2, 4	Y	13	6	254	0	3706 ± 121	3.70 ± 0.21	<1.90	26.3 ± 2.2	0.22 ± 0.04
J04144786+2648110	CX Tau	8.8	M2.5	II	1, 2, 3, 4	N	16	2	152	0	3520 ± 180	3.61 ± 0.30	<1.39	20.5 ± 2.5	0.28 ± 0.08
J04173372+2820468	CY Tau	8.6	M2.3	II	1, 2, 3, 4	N	16	2	203	0	3445 ± 155	3.73 ± 0.28	<1.31	10.8 ± 2.3	0.81 ± 0.13
J04183158+2816585	CZ Tau	9.4	M4.2	II	1, 2, 3, 4	Y	18	4	220	1	3385 ± 211	3.83 ± 0.35	<1.70	31.4 ± 3.1	0.64 ± 0.12
J04183112+2816290	DD Tau	7.9	M3.5	II	1, 2, 3, 4	Y	6	4	251	0	3250 ± 207	3.47 ± 0.37	<1.48	16.9 ± 3.1	1.82 ± 0.26
J04215563+2755060	DE Tau	7.8	M2.3	II	1, 2, 3, 4	N	16	4	251	0	3463 ± 158	3.45 ± 0.27	<1.01	9.4 ± 2.2	1.11 ± 0.11
J04270280+2542223	DF Tau	6.7	M2.0	II	1, 2, 3, 4	Y	24	4	293	3	⋯	⋯	⋯	⋯	⋯
J04270469+2606163	DG Tau	7.0	K7.0	II	1, 2, 3, 4	N	16	5	553	2	3969 ± 216	3.20 ± 0.28	<1.78	26.9 ± 4.3	4.82 ± 0.94
J04294155+2632582	DH Tau	8.2	M2.3	II	1, 2, 3, 4	N	16	10	399	0	3477 ± 125	3.89 ± 0.22	2.21 ± 0.32	8.4 ± 2.1	1.24 ± 0.10

Note. Columns 1–8 provide target information from the literature, while Columns 9–16 present information and parameters from this work. The Ref column identifies the source of the class and binary (objects with companions closer than 2″) classification. The SpT and the K magnitude come from Luhman et al. (2017) and Cutri et al. (2003), respectively. Uncertainties are the 1σ total (fit + systematic) uncertainties. The N column is the number of epochs combined for each object. The SNR$_{\rm K}$ column is the median SNR of the combined spectrum for the spectral regions used in this work. The flag column equals 0, 1, 2 or 3 indicating good, acceptable, outside/edge of grid, or poor determinations.

References. (1) Kenyon & Hartmann (1995); (2) Luhman et al. (2010); (3) Rebull et al. (2010); (4) Esplin et al. (2014); (5) Kraus et al. (2017); (6) Bouvier et al. (1992); (7) Correia et al. (2006); (8) Duchêne et al. (1999); (9) Dyck et al. (1982); (10) Ghez et al. (1993); (11) Haas et al. (1990); (12) Herbig & Bell (1988); (13) Ireland & Kraus (2008); (14) Konopacky et al. (2007); (15) Kraus et al. (2006); (16) Kraus et al. (2011); (17) Leinert et al. (1991); (18) Leinert et al. (1993); (19) Mathieu et al. (1991); (20) Mathieu et al. (1996); (21) Richichi et al. (1999); (22) Ruíz-Rodríguez et al. (2016); (23) Schaefer et al. (2014); (24) Simon et al. (1992); (25) Walter et al. (1988); (26) Weintraub (1989).

(This table is available in its entirety in machine-readable form.)
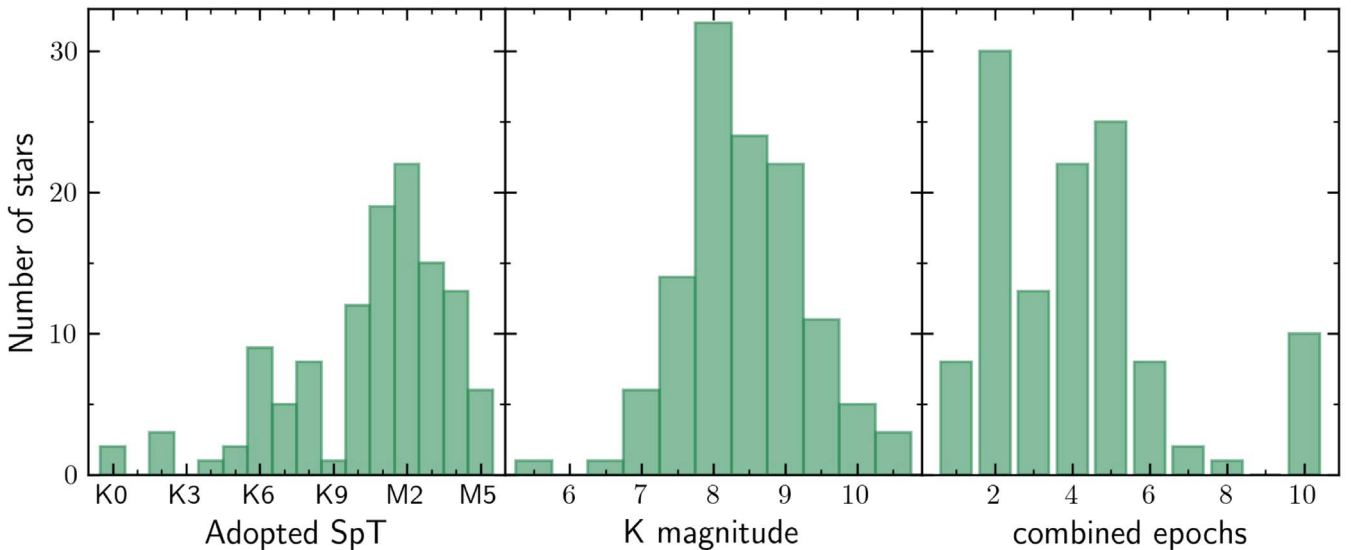
Figure 1. Luhman et al. (2017) spectral types (left panel), 2MASS K-band magnitudes (middle panel), and the total number of combined epochs (right panel) for our sample of 119 YSOs. More than 70% of the stars in our sample have spectral type K9 or later. Our sample also has a mean K magnitude of 8.4 ± 0.9 mag and a median value of 4 combined epochs per target.

All spectral lines depend, to some extent, on each of the stellar parameters. Isolating the contribution to the line profile of each parameter is only as accurate as the models and line lists. To reduce degeneracies, it was important to use a collection of spectral lines that are primarily sensitive to variations of just one stellar parameter.

To assess the sensitivity of the selected spectral regions to the stellar parameters, we took the difference between two synthetic spectra varied by 300 K in $T_{\rm eff}$, 0.5 dex in log g or 1.0 kG in B. Figure 2 depicts the dependency of each spectral region on the stellar parameters. We label the four intervals as follows:

Na region (2.2045–2.2105 μm): the Na doublet ($\lambda \sim 2.2062$ and 2.2090 μm) is the dominant feature of this region, but two Sc I lines (~ 2.2058 and 2.2071 μm) and a Si I line (~ 2.2068 μm) are also present. The Na lines show sensitivity to the magnetic field, while the Sc I and Si I are more sensitive to $T_{\rm eff}$ and respond in opposite ways as $T_{\rm eff}$ increases.

Ti region (2.2205–2.2346 μm): this region has three Ti I lines at ~ 2.2217, ~ 2.2239 μm, and ~ 2.2315 that are mainly sensitive to B. There are also two Fe I lines mainly sensitive to changes in $T_{\rm eff}$. The Ti lines present greater Zeeman splitting when the B field increases.

Ca region (2.2606–2.2664 μm): this region includes three Ca I lines at ~ 2.2614, 2.2631, and 2.2657 μm and one Fe I at ~ 2.2626 μm. These lines together help us to determine $T_{\rm eff}$ and log g because their dependency on B is small.

CO region (2.2986–2.3036 μm): this region contains six CO lines sensitive to log g and a weak Sc I line (~ 2.2993 μm) sensitive to B. As the log g increases the CO line depths decrease. This CO region is smaller than what others have used, which provides better continuum flattening.

The combined use of the four regions located in the K band allows for the accurate simultaneous determination of $T_{\rm eff}$, log g, B, and $v \sin i$ of our YSOs sample.

3.3. Determining Stellar Parameters

To determine stellar parameters we continuum-normalized each spectral region through an interactive python script. First,

the wavelength range of the spectral region is equally divided into n bins. Then, we computed the median ($\mu_{\rm flux}$) and the standard deviation ($\sigma_{\rm flux}$) of the flux in each bin; we then excluded points out of $\mu_{\rm flux} \pm 0.5\sigma_{\rm flux}$, and we recomputed the median flux of the bin ($\mu_{\rm clip}$). Finally, we fit a polynomial of order k to the $\mu_{\rm clip}$ of the n bins. The values of n and k vary between objects and spectral regions and could be interactively modified to obtain a better normalization. We typically used between 10 and 20 bins and between 1 and 4 for the polynomial order.

Then, we carried out an MCMC analysis, as implemented in the code *emcee* (Foreman-Mackey et al. 2013), using the four K-band spectral regions (Na, Ti, Ca, and CO). We compared observed and synthetic spectra by allowing $T_{\rm eff}$, log g, B, $v \sin i$, and K-band veiling ($r_{\rm K}$) to vary along with small continuum ($<3\%$) and wavelength (<0.6 Å) offsets. In each MCMC trial we linearly interpolated within the four-dimensional ($T_{\rm eff}$, log g, B, $v \sin i$) synthetic spectral grid described in Section 3.1, to obtain the corresponding spectrum with the sampled set of parameters. The interpolated synthetic spectrum was then artificially veiled and re-normalized for each region following this equation:

$$F_v = \frac{F + r_{\rm K}}{1 + r_{\rm K}} \quad (1)$$

where F_v, F, and $r_{\rm K}$ are the veiled flux, the synthetic flux, and the K-band veiling value (Basri & Batalha 1990). A single, best-fit veiling value was determined for all the K-band wavelength regions at once. Note that the $r_{\rm K}$ values determined with our MCMC analysis are not strictly a veiling value, but a combination of the true veiling with secondary systematic offsets between the model and target continua.

We then evaluated each MCMC with a likelihood function based on the sum of the χ^2 statistics divided by the number of pixels in each region. Finally, from the posterior probability distributions of the MCMC, we took the 50th percentile as the most likely value for the stellar parameters.
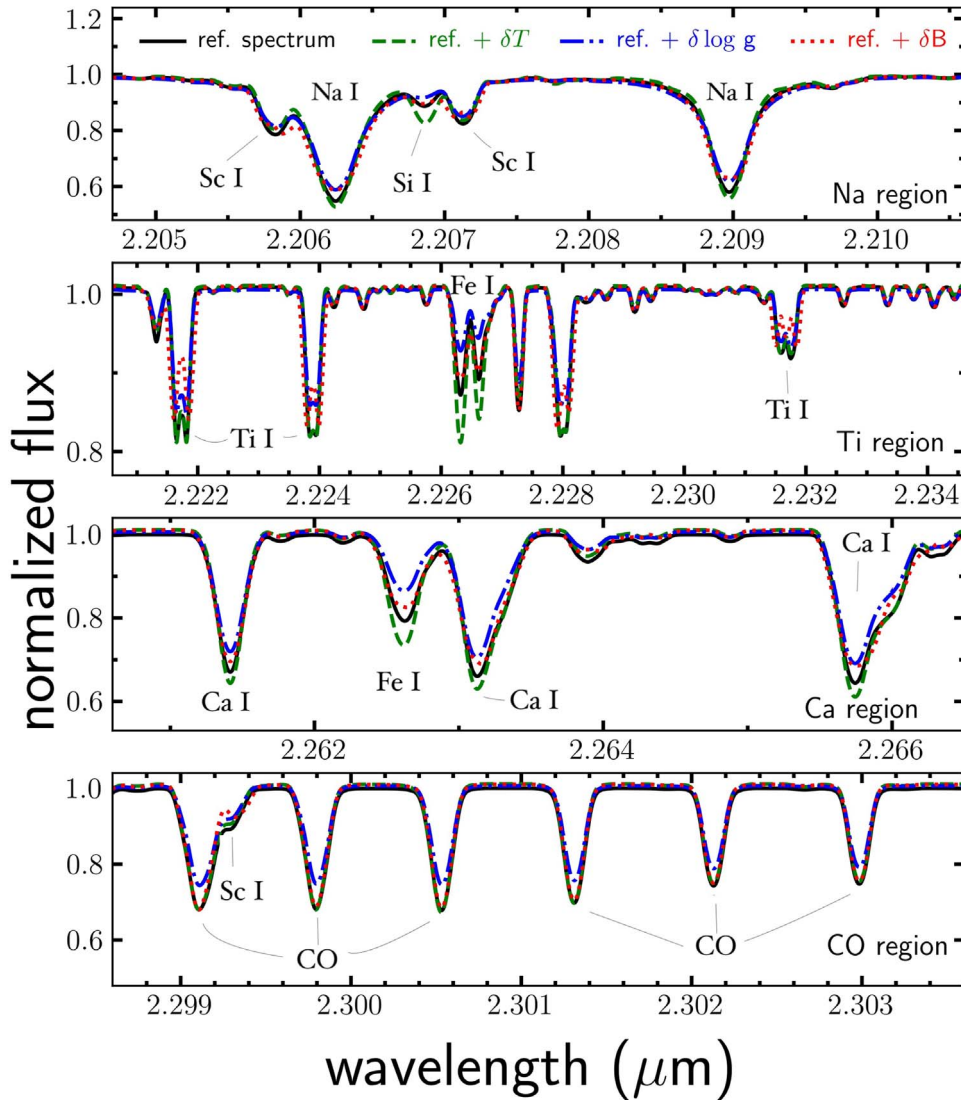
Figure 2. Dependence on stellar parameters for the selected spectral regions. We used a synthetic spectrum with $T_{eff} = 3600$ K, $\log g = 4.0$ dex, B = 2.0 kG, and $v \sin i = 10$ km s^{-1} (solid black line) as our reference. We show the difference caused by a change of 300 K in T_{eff} (green dashed line), of 0.5 dex in $\log g$ (blue dashed–dotted line), or 1.0 kG in B (red dotted line). In each comparison, we fixed two of the three parameters to the reference value and varied the third to a higher value. Varying parameters to lower values results in similar behavior in the opposite directions. A similar comparison can be seen in Sokal et al. (2018).

In Figure 3, we show the posterior distributions of the MCMC analysis for the star IW Tau as an illustrative example. Figure 3 also shows the dependence between stellar parameters like $\log g$ and r_K. A good fit to the observation can be achieved with a slightly lower $\log g$, or a higher r_K because both $\log g$ or veiling varies the CO line depths. The degeneracy between these parameters adds to the uncertainty in each quantity separately.
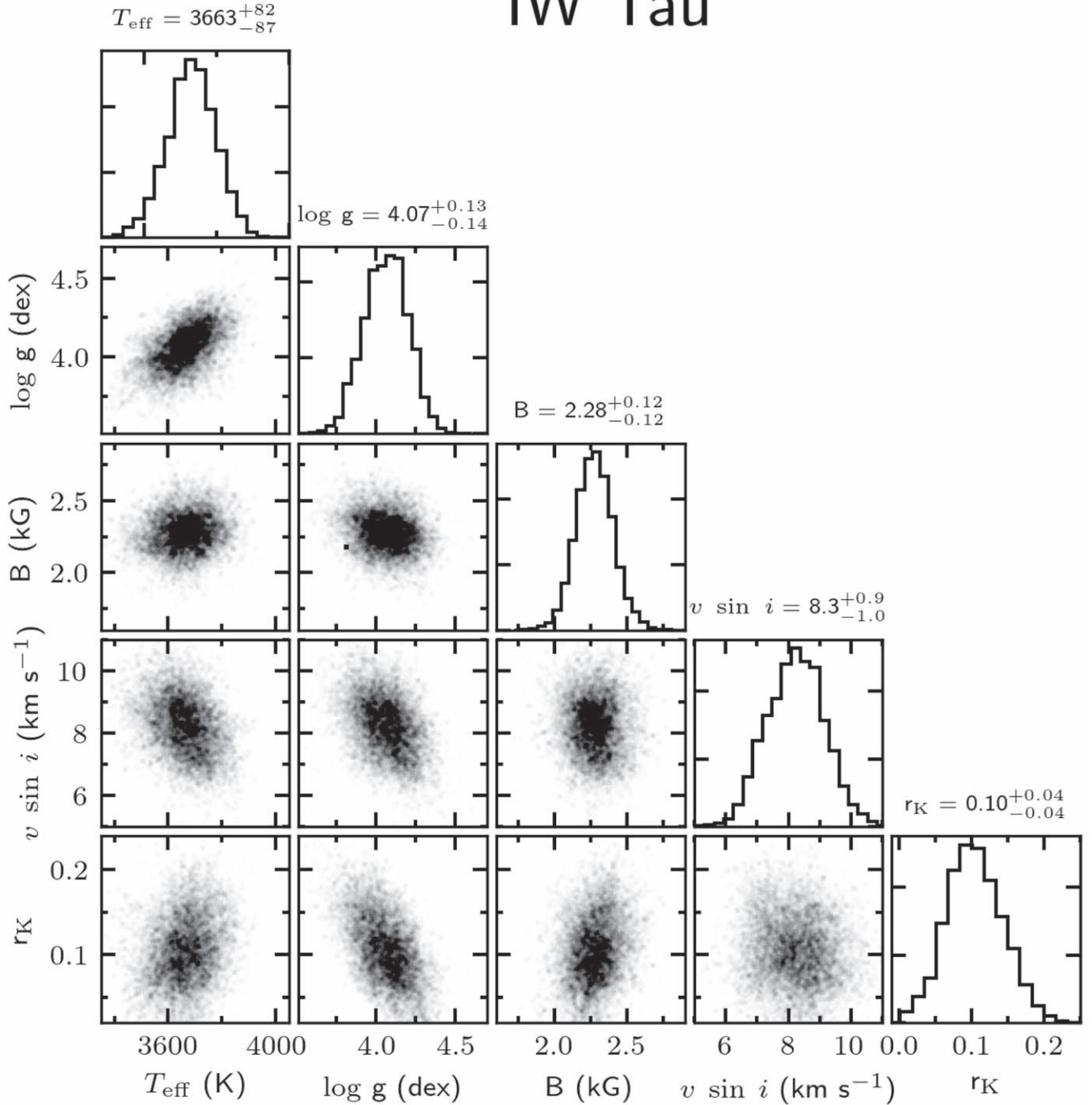
3.4. Uncertainties

The 16th and 84th percentiles of the posterior probability distributions of the stellar parameters represent the formal uncertainties of our fitting method. Most of the uncertainties were found to be nearly symmetric, and we report the larger of the two percentiles as the corresponding symmetric uncertainty (σ_{fit}) for each parameter. The median fit uncertainties are 152 K in T_{eff}, 0.25 dex in $\log g$, 0.54 kG in B, 1.9 km s^{-1} in $v \sin i$, and 0.10 in r_K.

Additionally, we quantified the systematic uncertainties (σ_{sys}) by comparing our stellar parameters to previously published values. Stars with precise physical parameters provided by interferometric observations help mitigate model dependency by calibrating relationships between T_{eff} and stellar radius. The works of Mann et al. (2013, 2015) and Newton et al. (2015) used 20+ stars with interferometric measurements to calibrate their model-independent relationships with $\sim$150 K precision. To quantify the σ_{sys} for T_{eff} and $\log g$, we determined the stellar parameters of seven field M stars with metallicity close to the solar value ([Fe/H] $= 0.0 \pm 0.10$ dex) from Mann et al. (2013).

We used the same fitting routines as for the YSO sample, but assuming $r_K = 0.0$ since these stars are on the main sequence and diskless. In Table 2, we compared our T_{eff} and $\log g$ values with those obtained by Mann et al. (2013). They determined T_{eff}, [Fe/H], mass (M), and radius (R), which we used in the

IW Tau

Figure 3. Posterior distributions and degeneracies (after removing the burn-in phase) of $T_{\rm eff}$, log g, B, $v \sin i$, and $r_{\rm K}$ determined for IW Tau. The median value and the 1σ uncertainties are listed above each distribution.

following equation to compute their log g values:

$$\log g_{\rm cal} = \log(M/M_{\odot}) - 2\log(R/R_{\odot}) + 4.437 \qquad (2)$$

We found an average difference in log g (ours—Mann) of -0.04 dex and a standard deviation of the residuals of 0.13 dex. For $T_{\rm eff}$ we found a mean difference of -69 K and a standard deviation of the residuals of 75 K. Therefore, we assigned 0.13 dex and 75 K as the systematic uncertainties for log g and $T_{\rm eff}$, respectively.

To obtain the systematic uncertainty on $v \sin i$, we compared measurements for 52 YSOs in common with Nofi et al. (2021). In that work, they determined the $v \sin i$ of pre-main-sequence stars using the same single-epoch, uncombined IGRINS K-band spectra that we have used. Their method used the cross correlation technique outlined in Hartmann et al. (1986) and Soderblom et al. (1989) along with synthetic spectra. In brief, a stellar spectrum with rotationally broadened lines was cross correlated against an unbroadened spectrum. Then the width of the cross correlation function is used to measure the rotational broadening of the spectrum. Generally, our $v \sin i$ values were

Table 2
Effective Temperature and Surface Gravity Determined for Our Calibration Sample as Well as Those Determinations of Mann et al. (2013)

Star	Mann et al. (2013)		This Work	
	$T_{\rm eff}$ (K)	log g (dex)	$T_{\rm eff}$ (K)	log g (dex)
GJ 338A	3953 ± 41	4.71 ± 0.05	3813 ± 56	4.68 ± 0.09
GJ 338B	3926 ± 37	4.72 ± 0.04	3785 ± 54	4.69 ± 0.08
GJ 436	3520 ± 66	4.77 ± 0.06	3587 ± 59	4.90 ± 0.11
GJ 570A	4588 ± 58	4.57 ± 0.07	4536 ± 50	4.36 ± 0.11
GJ 702B	4475 ± 33	4.66 ± 0.04	4391 ± 38	4.50 ± 0.14
GJ 809	3744 ± 27	4.72 ± 0.04	3604 ± 63	4.59 ± 0.09
GJ 887	3695 ± 35	4.78 ± 0.05	3699 ± 67	4.95 ± 0.08

Note. The fit errors are reported on our $T_{\rm eff}$ and log g determinations.

in good agreement with those of Nofi et al. (2021). We found a mean difference between the $v \sin i$ values (ours—Nofi) of 0.2 km s^{-1} and a standard deviation of the residuals of 1.7 km s^{-1}. We assigned this 1.7 km s^{-1} as the $v \sin i$ systematic uncertainty.

Over 85% of our $v \sin i$ values are ⩽30 km s^{-1}, with the median value being 16.6 km s^{-1}. In Figure 4 we compare $v \sin i$ measurements for 60 YSOs in common with Nguyen et al. (2012). They used high-resolution ($R = 60,000$) optical (4800–9300 Å) spectra to determine $v \sin i$ for pre-main-sequence stars in the Chamaeleon I and Taurus-Auriga star-forming regions. Their method compared each echelle order of the target spectrum with slow-rotating template stars, which were artificially broadened to different values of $v \sin i$ to find the best fit. Finally, they removed 2.7σ outliers around the mean value and computed a weighted average over all the remaining echelle orders (for more details, see also Nguyen et al. 2009). We found our $v \sin i$ values in agreement with those of Nguyen et al. (2012), with a mean difference of 0.08 km s^{-1} and a error on the mean of 0.3 km s^{-1}.

Finally, we collected 12 determinations (for 11 YSOs) of B-field strength from the literature (Johns-Krull 2007; Sokal et al. 2020; Flores et al. 2020) to assess the systematic uncertainty of our B values (see Table 3). We found a mean difference in the residuals (ours—literature) of −0.27 kG and a standard deviation of 0.26 kG. We assigned 0.26 kG as our systematic uncertainty in the B-field measurements.

The systematic uncertainties were added in quadrature to the fit errors to compute the total error of each parameter ($\sigma_{\rm tot}$), which we report in Table 1.

4. Results and Analysis

We plotted the spectral regions used in our analysis for all the observed and the best-fit spectra, as in Figure 5, to categorize the quality of our parameter determinations. Through a ranking of the χ^2 statistics and visual inspection, we marked each set of parameters in Table 1 with a numerical flag equal to 0, 1, or 3 if they were good, acceptable, or poor determinations, respectively. We also computed the lower and upper limits of each parameter using its total uncertainty to look for values outside or at the edge of our grid. We find that six lower limits of log g meet this criterion. We flagged these parameters with a flag equal to 2 and have retained these measurements in our analysis since they are otherwise classified as "good" determinations. We found that our
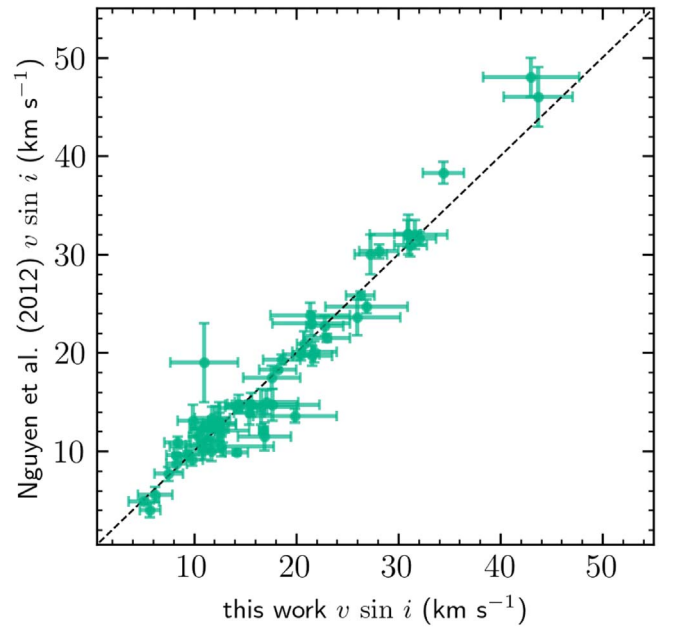
Figure 4. Comparison of $v \sin i$ values between Nguyen et al. (2012) and this work for 60 YSOs in common. The dashed line shows the one-to-one relation. The mean difference between both studies is 0.08 ± 0.3 km s^{-1}, and we found a correlation coefficient of 0.97. Our error bars are the fit uncertainties.

Table 3
Literature and This Work Magnetic-field Strength Determinations for 11 YSOs

| Star	B Literature (kG)	Ref.	B This Work (kG)
AA Tau	2.78 ± 0.28	JK07	2.16 ± 0.32
BP Tau	2.17 ± 0.22	JK07	2.19 ± 0.27
BP Tau	2.50 ± 0.16	F19	2.19 ± 0.27
CI Tau	2.15 ± 0.15	S20	1.95 ± 0.16
CY Tau	1.16 ± 0.12	JK07	1.31 ± 0.37
DE Tau	1.12 ± 0.11	JK07	1.01 ± 0.24
DH Tau	2.68 ± 0.27	JK07	2.21 ± 0.18
DK Tau	2.64 ± 0.26	JK07	2.55 ± 0.58
DN Tau	2.00 ± 0.20	JK07	1.54 ± 0.26
GI Tau	2.73 ± 0.27	JK07	1.92 ± 0.36
GK Tau	2.28 ± 0.23	JK07	2.05 ± 0.87
GM Aur	2.22 ± 0.22	JK07	2.11 ± 0.22

Note. The reference column are JF07 = Johns-Krull (2007), F19 = Flores et al. (2019), and S20 = Sokal et al. (2020). We report the fit uncertainties on our B values.

parameter determination method needs a minimum median SNR ⩾ 80 to produce reliable results. A median SNR ⩾ 150 is generally required for good parameter determinations. In total, we identified 80, 24, 9, and 6 stars whose parameters are good, acceptable, poor, and outside/edge of grid, respectively. We exclude poor determinations in further analysis, and we will refer to the 110 remaining YSO measurements as our Taurus sample.

4.1. Magnetic Fields

While Zeeman line-splitting effects are most significant in the Ti region, the Na region is also sensitive to variations in the B field (see Figure 2). However, our ability to measure Zeeman line separations is primarily a function of the line widths, which are dominated by $v \sin i$. Hussaini et al. (2020) measured the
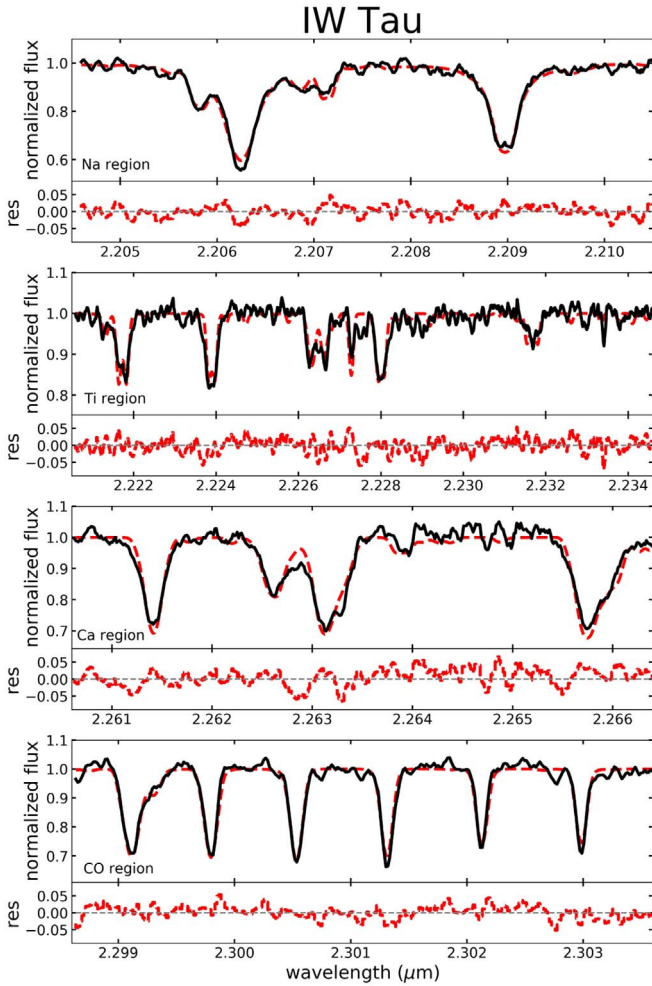
Figure 5. The four IGRINS K-band spectral regions of the star IW Tau (solid black line). We include the best-fit synthetic spectrum (red dashed line) with $T_{\rm eff} = 3663$ K, log $g = 4.07$ dex, B = 2.28 kG, $v \sin i = 8.3$ km s^{-1}, and $r_{\rm K} = 0.10$. In the bottom panels, we present the residuals between the observed and the synthetic spectra. The level of agreement between the best-fit-parameter synthetic spectrum and the IW Tau observed spectrum was considered a good determination.

line splitting of the Na and Ti spectral regions in IGRINS data and the MOOGSTOKES spectra employed in this work. That work found that the retrieval of B is limited to $\sim v \sin i / 10$ in the Ti region and $\sim v \sin i / 5$ in the Na region. In other words, an object with $v \sin i = 15$ km s^{-1} must have B > 1.5 kG for Zeeman splitting to be measurable in the Ti region and >3 kG to be measurable in the Na region. Additionally, the IGRINS spectral resolution limits the minimum measurable B field from line splitting to ~ 0.7 kG. For this work, we conservatively considered a detection limit of B $\geqslant (v \sin i / 8)$ kG, and no lower than 1 kG. Values of B field lower than 1 kG cannot be distinguished from a non-detection at the spectral resolution of IGRINS when simultaneously fitting for other model parameters. We found that 41 of our B-field determinations meet the detection threshold. The remaining upper-limit measurements are provided in Table 1.

4.2. Impact of B on the Stellar Parameters

To evaluate the impact of B on $T_{\rm eff}$, log g, $v \sin i$, and $r_{\rm K}$, we fixed B to 0 kG and redetermined the stellar parameters for the 41 YSOs with B-field detections in Table 1. In Figure 6 we

compare the stellar parameters determined in our primary analysis with those obtained by disabling the B parameter. We further consider the low-B (objects with B $\leqslant 2$ kG) and the high-B (B > 2 kG) results in this comparison.

We found that all the $T_{\rm eff}$ values determined without considering the B-field effects are systematically colder than those found considering the B-field. For low B (18 objects), we found a mean difference of -42 ± 4 K, while for high B (23 objects), this difference increases slightly to -73 ± 9 K. Both values are well within the median total (fit+systemic) $T_{\rm eff}$ error, which is ~ 170 K. Similarly, $r_{\rm K}$ is lower when B is not taken into account, with a mean difference of -0.14 ± 0.02 for both the low- and high-B bins. Contrary to $T_{\rm eff}$ and $r_{\rm K}$, most of the log g values are higher by 0.08 ± 0.01 dex and 0.03 ± 0.01 dex for the low- and high-B bins, respectively, when not considering B fields in the fit. These log g differences are within the log g median total (fit+systemic) error of 0.28 dex. It is likely that the degeneracy between log g and $r_{\rm K}$ discussed in Section 3.3 is why log g is overestimated and $r_{\rm K}$ is underestimated when B is not included in the parameter determinations.

The most prominent effect of ignoring the B-field strength when determining parameters is seen in the $v \sin i$ values. All $v \sin i$ determinations are higher without the B field included in the fit and the difference is greater for larger values of B. We found for the low-B bin a mean difference of 1.6 ± 0.2 km s^{-1}. For the high-B bin, the difference increases to 3.8 ± 0.3 km s^{-1}. This trend is explained by excess rotational broadening of the synthetic spectral lines to try and replicate the B-field-induced Zeeman line-splitting. The absence of B-field considerations by Nguyen et al. (2012) and Nofi et al. (2021) is likely responsible for some of the differences between those works and ours, which adds to the systematic uncertainties.

The previous tests suggest that it is possible to obtain suitable stellar parameters, even when excluding the B field from the determination. However, the parameters will have systematic offsets, with magnetically active YSO parameters being the most impacted.

4.3. Effective Temperature

Kenyon & Hartmann (1995) presented a conversion between spectral type and $T_{\rm eff}$ for young stars, based on the work of Schmidt-Kaler (1982) and Straižys (1992). Shortly after, Luhman (1999) developed a new temperature scale for young M stars between the giant and dwarf scales. However, improvements made in the last two decades in the modeling of cool star atmospheres, and the development of new instruments, have resulted in several studies that have determined effective temperatures (or spectral type) either for field (e.g., Casagrande et al. 2008; Rajpurohit et al. 2013; Rajpurohit et al. 2018; López-Valdivia et al. 2019) or for young (e.g., Luhman et al. 2003a; Luhman et al. 2003b; Herczeg & Hillenbrand 2014; Cottaar et al. 2014; Yao et al. 2018) K and M stars.

In Figure 7 we compare the $T_{\rm eff}$ values we determined to spectral types from Luhman et al. (2017), along with three different temperature scales of pre-main-sequence stars (Luhman et al. 2003b; Herczeg & Hillenbrand 2014; Pecaut & Mamajek 2013). To analyze how multiplicity plays a role in determining $T_{\rm eff}$, we divided our sample into single (51) and binary (44) stars based on classifications from the literature.
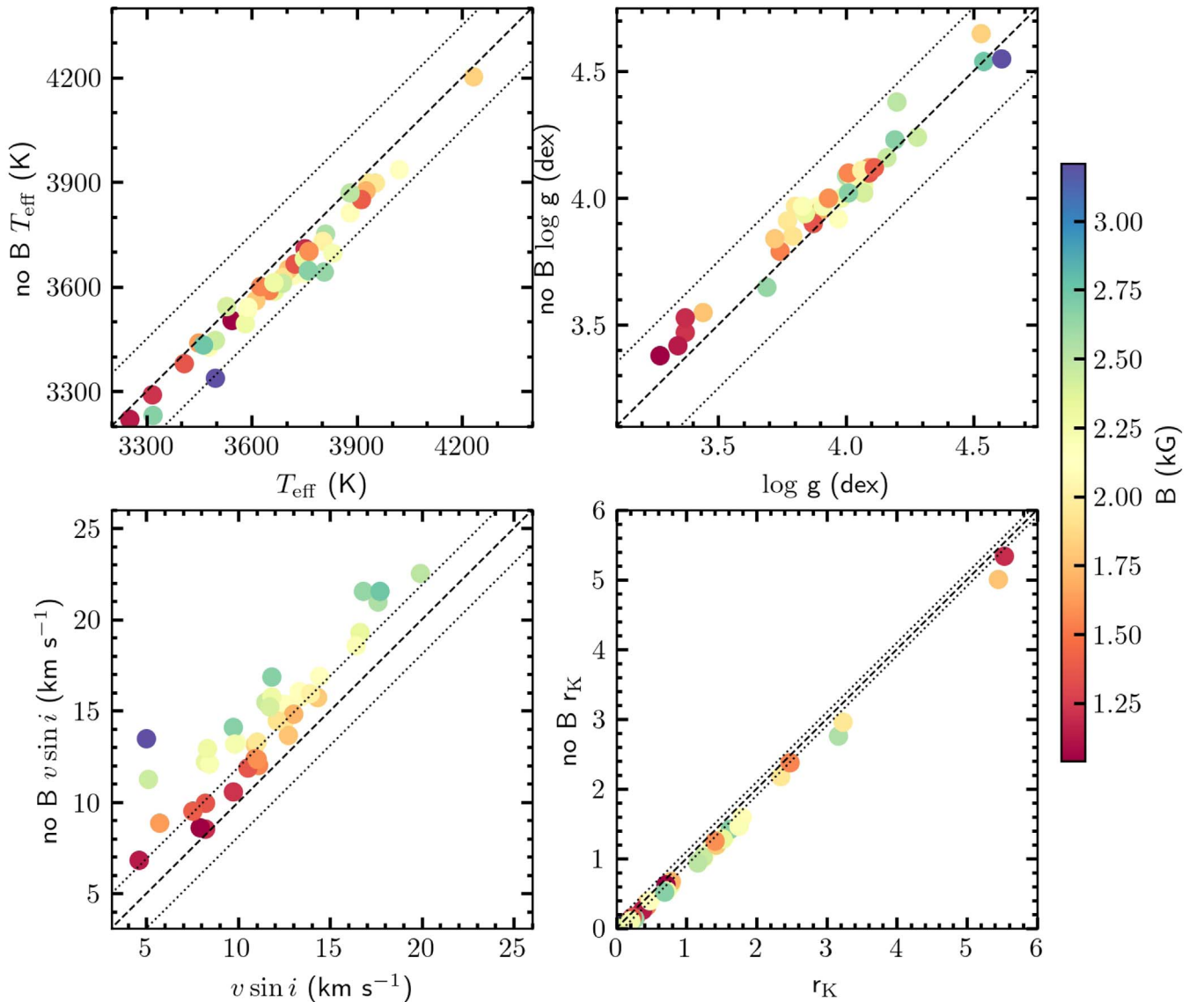
Figure 6. Stellar parameters determined with and without taking into account the effects of B-field strength. The dashed line is the one-to-one relation, while the dotted lines demarcate the median fit error intervals, namely: ± 150 K, ± 0.25 dex, ± 1.9 km s^{-1}, and ± 0.10 for $T_{\rm eff}$, log g, $v \sin i$, and $r_{\rm K}$, respectively. The data are color-coded by the determined strength of B.

These identifications are reported in Table 1. We consider a star a binary if it has a companion closer than 2 arcseconds because the resultant IGRINS spectrum will contain some amount of flux from both components.

The amount of contamination from a binary companion is not easily quantified. An equal brightness binary with no velocity offsets will have composite line profiles, often producing poor fits to the data. If the binary has equal brightness and radial velocity offsets (a double-lined spectroscopic binary), then line blending in the combined spectrum will often result in poor parameter determinations. Generally, equal brightness binaries have been excluded from our analysis by visual inspection in the initial sample selection and at the parameter-fit quality check. Binaries with disproportionate fluxes will have the same issues as equal-flux binaries, but at lower levels. Stellar parameters obtained for the known binary stars should be used with caution since secondary contamination is possible, although the spectral fit is dominated by the primary star's contribution. The binary identification here allows us to look for systematic differences in the data.

In general our temperatures follow the scales of Pecaut & Mamajek (2013), Herczeg & Hillenbrand (2014), and Luhman et al. (2003b) for both the single and binary samples. Early K-type binaries (T Tau, RW Aur, and HQ Tau) show large discrepancies which is possibly due to wrong SpT classifications as Flores et al. (2020) also found a cooler temperature for T Tau ($T_{\rm eff} = 3976 \pm 90$ K), cool spots, or the binary nature of these YSOs' biasing measurements to cooler temperatures. A more detailed multi-epoch and multi-wavelength study should be carried out at higher angular resolution to understand the large variation in temperatures for these early-K binaries.

A temperature scale for the single stars was computed using the mean value and the standard deviation within ± 0.5 spectral type sub-classes bins. This IGRINS temperature scale, reported in Table 4, represents an alternative to previously published pre-main-sequence stars' temperature scales, with the advantage of being obtained through a simultaneous determination of
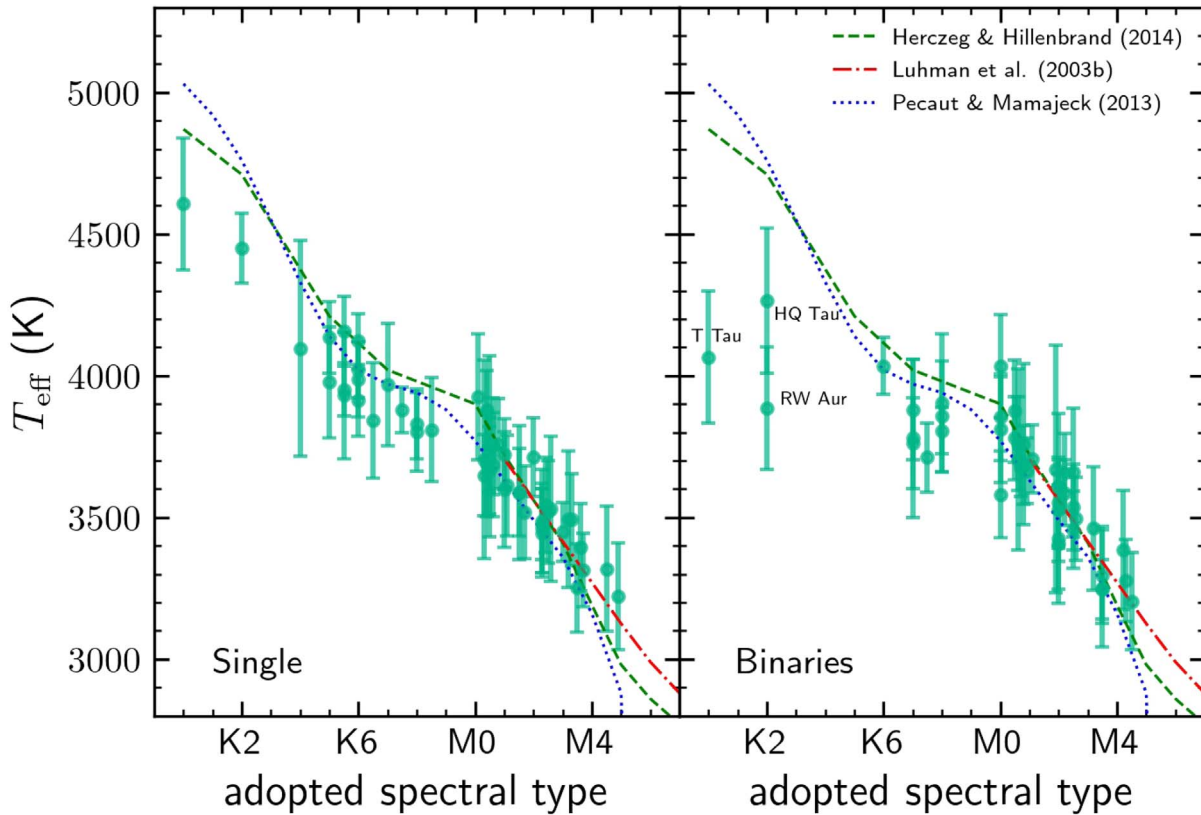
Figure 7. Effective temperature as a function of Luhman et al. (2017) spectral type for our Taurus-Auriga known single and binary (multiple) YSOs. The dashed, dotted–dashed, and dotted lines are the temperature scales of Herczeg & Hillenbrand (2014), Luhman et al. (2003b), and Pecaut & Mamajek (2013), respectively. Typically the error on the spectral type is about 1 subclass. There is good agreement between our temperatures for M0–M4 single and K6–M5 binary stars with the published temperature scales. For single K stars, our $T_{\rm eff}$ values are cooler than the published temperature scales. The binary stars HQ Tau, T Tau, and RW Aur present the largest discrepancies. Our error bars are the total (fit + systematic) $T_{\rm eff}$ uncertainties.

Table 4
Temperature Scales of Luhman et al. (2003b, L03), Pecaut & Mamajek (2013, PM13), Herczeg & Hillenbrand (2014, HH14) and Those Determined in This Study for Single YSOs

SpT	L03 (K)	PM13 (K)	HH14 (K)	This Work (K)	N
K0	⋯	5030	4870	4606 ± 233	1
K2	⋯	4760	4710	4450 ± 123	1
K5	⋯	4140	4210	4055 ± 78	2
K7	⋯	3970	4020	3905 ± 63	2
M0	⋯	3770	3900	3769 ± 111	5
M1	3705	3630	3720	3696 ± 56	9
M2	3560	3490	3560	3535 ± 79	9
M3	3415	3360	3410	3496 ± 26	5
M4	3270	3160	3190	3319 ± 58	3
M5	3125	2880	2980	3269 ± 48	2

Note. The last column corresponds to the number of objects with which we computed the mean $T_{\rm eff}$ value and the standard deviation within a ± 0.5 spectral-type sub-classes. If just one object was included in the spectral-type bin, we report the value of $T_{\rm eff}$ (and its error) found in our analysis.

various atmospheric parameters and the inclusion of the magnetic-field effects.

4.4. Surface Gravity, Stellar Ages, and Masses

The log g–$T_{\rm eff}$ plane, also known as the spectroscopic Hertzsprung–Russell diagram (sHR; Langer & Kudritzki 2014), helps estimate stellar properties such as age and mass because log g and $T_{\rm eff}$ are proxies for those properties (see Figure 9 of Sokal et al. 2018). According to the evolutionary models of Baraffe et al. (2015), over the mass range of 0.05–1.4 $M_\odot$, the log g changes by about 0.5 dex between 1 to 10 Myr. Therefore, two populations of different ages should occupy different parts of the sHR.

With this in mind, we observed members of the TW Hydrae Association (TWA; Kastner et al. 1997). TWA is a nearby (∼60 pc; Zuckerman & Song 2004; Gaia Collaboration et al. 2018) and young (∼7–10 Myr; Ducourant et al. 2014; Herczeg & Hillenbrand 2015; Sokal et al. 2018) group of stars that serves as an evolved counterpart to our Taurus sample. We analyzed and determined the stellar parameters (Table 5) for all 19 TWA objects in the same fashion as the Taurus sample. In Figure 8 we assemble the sHR of the Taurus and TWA YSOs and compare them to the 1, ∼5, and 10 Myr isochrones of Baraffe et al. (2015).

As expected, the Taurus and TWA YSOs populate different parts of the sHR, exhibiting an offset in log g. Most of the Taurus sample is located between the 1 and 5 Myr isochrones while the TWA members are located below the 5 Myr isochrone. We found a mean log g (and error on the mean) of 3.87 ± 0.03 dex and 4.22 ± 0.03 dex, for Taurus and TWA, respectively.

We applied to the log g distributions of Taurus and TWA a Kolmogorov–Smirnov (KS) test.[14] The KS test explores the

---

[14] We have used the KS_2samp function, which is part of the python package Scipy.stats.

Table 5
Stellar Parameters and Basic Information for 19 TWA Members

2MASS ID	Name	SpT	Ref.	K (mag)	flag	$T_{\rm eff}$ (K)	log g (dex)	B (kG)	$v \sin i$ (km s^{-1})	$r_{\rm K}$
J11015191-3442170	TWA 1	M0.5	1	7.3	0	3783 ± 108	4.35 ± 0.18	2.75 ± 0.30	8.4 ± 2.0	0.53 ± 0.05
J11091380-3001398	TWA 2	M2.2	1	6.7	0	3558 ± 92	4.07 ± 0.16	<1.38	15.9 ± 1.9	0.06 ± 0.02
J11102788-3731520	TWA 3A	M4.1	1	6.8	1	3285 ± 75	4.00 ± 0.13	<0.97	11.9 ± 1.7	0.29 ± 0.01
...	TWA 3B	M4.0	1	...	1	3355 ± 75	4.20 ± 0.13	<1.78	15.8 ± 1.7	0.16 ± 0.01
J11220530-2446393	TWA 4	K6.0	1	5.6	0	4257 ± 103	4.51 ± 0.21	<1.10	10.2 ± 2.1	0.31 ± 0.04
J10423011-3340162	TWA 7	M3.2	1	6.9	0	3328 ± 80	4.27 ± 0.13	2.19 ± 0.26	7.4 ± 1.7	0.10 ± 0.01
J11324124-2651559	TWA 8A	M2.9	1	7.4	0	3398 ± 75	4.30 ± 0.13	2.86 ± 0.26	7.5 ± 1.7	0.13 ± 0.01
J11482422-3728491	TWA 9A	K6.0	1	7.8	0	4043 ± 94	4.32 ± 0.17	2.29 ± 0.30	12.0 ± 2.0	0.17 ± 0.03
J11482373-3728485	TWA 9B	M3.4	1	9.2	0	3351 ± 75	4.30 ± 0.14	<1.30	10.9 ± 1.7	0.09 ± 0.01
J12350424-4136385	TWA 10	M3.0	2	8.2	1	3358 ± 75	4.23 ± 0.13	2.54 ± 0.26	9.5 ± 1.7	0.10 ± 0.01
J12360055-3952156	TWA 11B	M2.5	3	8.3	0	3532 ± 115	4.22 ± 0.18	2.23 ± 0.34	14.8 ± 2.1	0.02 ± 0.02
12354893-3950245,	TWA 11C	M4.5	2	8.9	1	3391 ± 122	4.45 ± 0.22	<1.98	22.8 ± 2.3	0.36 ± 0.04
J11210549-3845163	TWA 12	M2.75	2	8.1	0	3534 ± 104	4.19 ± 0.17	2.67 ± 0.32	19.7 ± 2.0	0.02 ± 0.02
J11211723-3446454	TWA 13A	M1.1	1	7.5	0	3638 ± 96	4.14 ± 0.16	2.12 ± 0.29	14.2 ± 1.9	0.04 ± 0.02
J11211745-3446497	TWA 13B	M1.0	1	7.5	0	3673 ± 93	4.13 ± 0.16	1.71 ± 0.30	13.7 ± 1.9	0.04 ± 0.02
J12345629-4538075	TWA 16	M3.0	2	8.1	0	3445 ± 91	4.15 ± 0.16	1.85 ± 0.28	12.4 ± 1.9	0.07 ± 0.02
J12072738-3247002	TWA 23	M3.5	1	7.8	1	3405 ± 101	4.15 ± 0.18	<1.42	19.1 ± 1.9	0.16 ± 0.03
J12153072-3948426	TWA 25	M0.5	1	7.3	0	3707 ± 99	4.14 ± 0.17	2.21 ± 0.29	15.0 ± 1.9	0.06 ± 0.03
J10120908-3124451	TWA 39	M4.0	4	8.0	1	3316 ± 88	4.06 ± 0.18	<1.34	18.0 ± 2.0	0.28 ± 0.03

Note. The quality flag is the same as in Table 1. K magnitudes come from 2MASS (Cutri et al. 2003) while the SpT references are indicated. The errors on the stellar parameters are the total (fit + systematic) uncertainties.
References. (1) Herczeg & Hillenbrand (2014); (2) Luhman et al. (2017); (3) Webb et al. (1999); (4) Riedel et al. (2014).

null hypothesis that two samples are drawn from the same distribution. If the probability value ($\mathcal{P}$(KS)) obtained from this test is higher than a certain threshold, often set at 1%, 5%, or 10%, we cannot reject the null hypothesis. We found a $\mathcal{P}$(KS) $\sim 10^{-8}$ that the log g distributions of Taurus and TWA come from the same parent distribution, validating that precise log g values can provide meaningful age proxies for populations of stars.

For the mean $T_{\rm eff}$ and log g values, and the set of isochrones from Baraffe et al. (2015), we can make a rough estimate of the age of Taurus and TWA. Our calculations lead to a Taurus mean age of ~2.5 Myr and a TWA mean age of ~10 Myr. However, the dispersion within these groups is larger than the differences between them. The parameters of the least evolved TWA members are more similar to the more evolved members of Taurus than to the most evolved members of TWA.

4.5. Class II versus Class III YSOs

Based on the shape of their spectral energy distributions, Adams et al. (1987) divided YSOs into three different morphological classes (I, II, and III) using the spectral index $n = d \log(\lambda F_\lambda)/d \log \lambda$, and suggested that such classes represent an evolutionary sequence in the formation of low-mass stars. Since then, the sequence has been extended to Class 0 YSOs embedded in an infalling cold dust envelope (Andre et al. 1993), flat-spectrum YSOs (Greene et al. 1994) between Class I and II, and post-Class III transition disk objects without the cold dust corresponding to flux from 5-20 μm (Lada et al. 2006). If the classification of YSOs by their SED slope, as suggested, represents an evolutionary scheme, the populations of YSOs would differ in terms of stellar properties, such as log g, given that stars undergo gravitational contraction while they evolve toward the main sequence (Herbig 1962).

To test this, we collected YSO classifications from the literature for 84 Class II and 35 Class III (78 and 32 with good or acceptable parameters, respectively) objects in our sample (Kenyon & Hartmann 1995; Luhman et al. 2010; Rebull et al. 2010; Esplin et al. 2014; Kraus et al. 2017). We used a KS test to quantify if the stellar parameters determined for the Class II and Class III stars are statistically different.

We found a $\mathcal{P}$(KS) of 32%, 9%, and 6% that the Class II and Class III objects come from the same parent distributions of $T_{\rm eff}$, $v \sin i$, and B respectively.[15] This probability dropped to values lower than 1% for log g and $r_{\rm K}$. These probability values indicate that the Class II and Class III YSOs of our sample are statistically indistinguishable in terms of $T_{\rm eff}$, marginally indistinguishable in terms of $v \sin i$ and B, but different in terms of $r_{\rm K}$ and log g.

The results of the KS tests for $T_{\rm eff}$ and $r_{\rm K}$ are not surprising. The distribution of temperatures (SpT) reflects the initial mass function of Taurus. Also, Class II YSOs host disks are actively accreting, which correlates with high levels of veiling, while Class III objects have lost their disks and show little or no veiling. The veiling values we measure for Class III objects are closer to zero than what we find for Class II YSOs, consistent with the expected behavior. For $v \sin i$, the $\mathcal{P}$(KS) of 9% that we found is in agreement with the findings of Nguyen et al. (2009), who found that low-mass accretors and non-accretors in Taurus have a $\mathcal{P}$(KS) = 10% of coming from the same $v \sin i$ parent distribution.

Since log g can be used as a proxy for age (Yao et al. 2018), the different distributions for Class II and Class III YSOs support the idea of an evolutionary sequence (see Figure 9). We found a mean log g of 3.83 ± 0.03 and 4.06 ± 0.04 dex for Class II and Class III Taurus objects, respectively. The most interesting sources in each log g distribution are those in the wings, where evolutionary differences between the lowest log g Class III YSOs and the highest log g Class II YSOs are still not well understood.

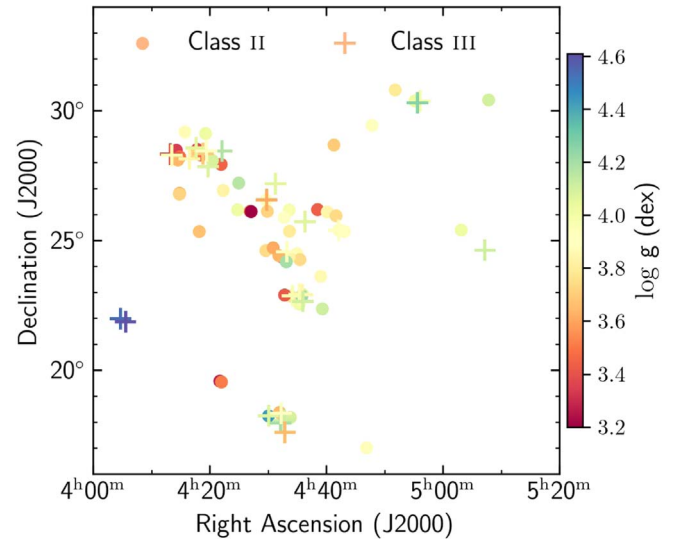[15] We considered just the 41 B determinations in this test, not the limits.
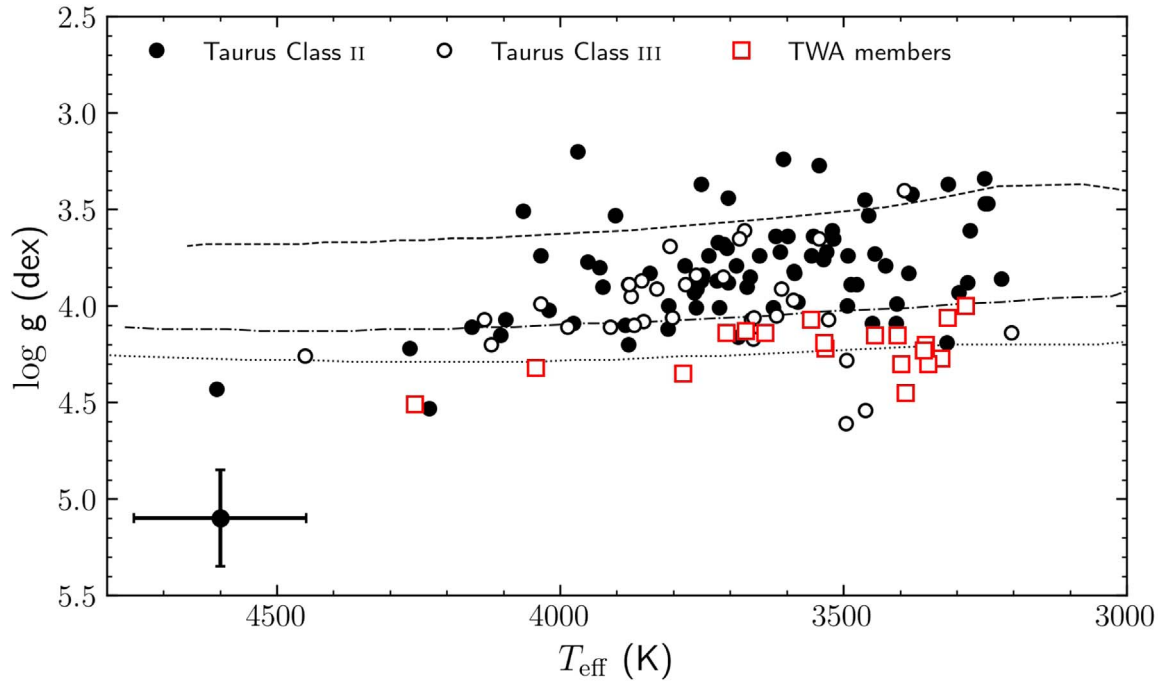
Figure 8. Spectroscopic Hertzsprung–Russell diagram. The solid and empty circles represent our determinations for Class II and Class III Taurus YSOs, while the empty squares are our determinations for the TWA members. These different YSO samples present an offset in log g, which suggests an age ladder with the Taurus YSOs being younger than their TWA counterparts. We also include the Baraffe et al. (2015) isochrones of 1 (dashed line), ~5 (dashed–dotted line) and 10 Myr (dotted line). The error bar represents our median fit uncertainties.
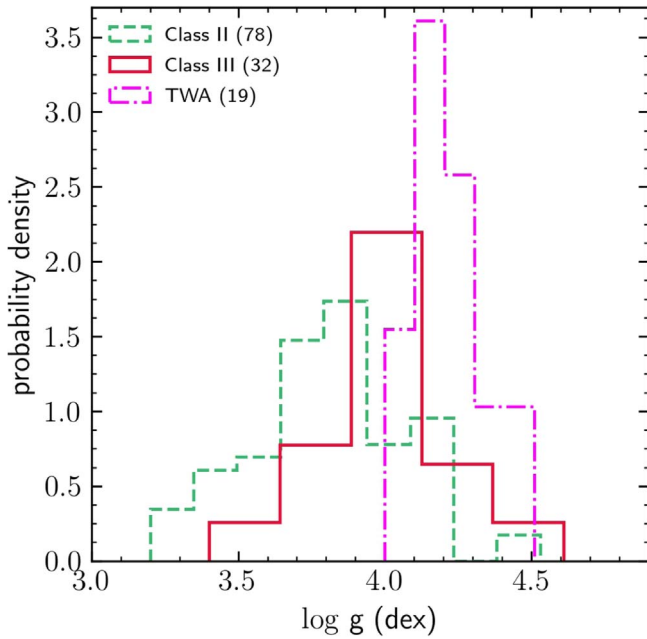
Figure 9. Probability densities of log g for 78 Class II (dashed) and 32 Class III (solid) Taurus YSOs. We also included the log g probability density of the TWA YSOs as a comparison. We computed a KS probability between the Class II and Class III of ~3 × 10^{-3}. If we compare the log g distributions of the Taurus and TWA YSOs, we also found low-KS probabilities of ~1.5 × 10^{-9} and ~7 × 10^{-5}, for Class II and Class III, respectively. These low-probability values show that Taurus Class II and Class III YSOs, as well as the TWA objects, are different in terms of their log g.

Figure 10. The spatial distribution of the Taurus sample color-coded by log g. The 78 Class II (circles) and 32 Class III (crosses) YSOs are distributed similarly across the sky. There is no significant clustering of Class II or Class III objects in the sample we have studied.

this is a two-dimensional view of Taurus and it will require the entire population of Taurus YSOs (>400; Luhman 2018) studied in the context of three-dimensional substructures (Krolikowski et al. 2021) before we can fully understand the spatial distribution in relation to the parameters we have determined.

4.6. Important Considerations

There are many ways to perform the parameter determination that we present here. As outlined above, there are a variety of

Finally, the spatial distribution for the IGRINS Taurus sample (Figure 10) does not show significant clustering of Class II or Class III objects, nor a trend with log g, suggesting that there is not a star formation gradient across the cloud. Yet,

models to choose from and possible approaches. We have shown that magnetic fields are a critical component of the parameter determination and we allowed many of the YSO parameters to remain variables in the fit rather than fixing them to assumed values. During our tests, we found that log g was the most sensitive parameter to variations in our approach. Additionally, we fit for all parameters simultaneously rather than taking an iterative approach to the fitting. While deciding on the best method for parameter determination, by minimizing fit residuals and validating the results against the literature, we have identified some important considerations when performing YSO parameter determinations.

Use of consistent $T_{\rm eff}$ estimators: IGRINS provides us with both the H- and K-band spectrum of our sources, but we have only employed the K-band in our analysis. There are temperature-sensitive spectral features in the H band (the OH region of López-Valdivia et al. 2019) that we initially included in our analysis. The result of including this H-band region was an offset in log g toward higher values, inconsistent with the evolutionary stage of the Taurus star-forming region. Using both the H- and K-band spectra meant that log g came primarily from the CO region and $T_{\rm eff}$ came from the OH region, which are about 0.7 μm apart. Furthermore, Gully-Santiago et al. (2017) found that $T_{\rm eff}$ varies as a function of wavelength when a single temperature component was fit to the IGRINS spectrum of the spotted YSO LkCa 4. The temperature in the CO region of LkCa 4 is ~700 K cooler than the value determined in the OH region (see Figure 3 of Gully-Santiago et al. 2017). In this work, differences between the H- and K-band temperatures were compensated for by the remaining stellar parameters, which primarily impacted the log g determination. While the broad spectral grasp of IGRINS permits the analysis of additional features, it also probes different components of the YSO photosphere, which can produce conflicting measurements. We have mitigated these effects by fitting only the K-band regions of the Taurus YSOs.

Degeneracy between $r_{\rm K}$ and log g: Another consideration was the degeneracy between log g and $r_{\rm K}$. As seen in the diagonal distribution of $r_{\rm K}$ and log g in the sub-panel of Figure 3, higher values of $r_{\rm K}$ result in lower log g values and vice versa. This degeneracy results in a fixed $T_{\rm eff}$ because $r_{\rm K}$ and log g impact the CO lines in nearly in the same way, and the CO lines are the most log-g-sensitive lines in our analysis. This degeneracy increases the uncertainties for each parameter and we conclude that log g and $r_{\rm K}$ need to be determined simultaneously and from the same spectrum. The use of fixed $r_{\rm K}$ or log g values from the literature will disproportionately impact the other parameter.

The atomic data: our method relies on the comparison of observed and synthetic spectra and the line list and the model atmosphere selected is a crucial component of the result. We initially determined the stellar parameters using the unmodified VALD line list expecting that the use of different spectral regions would average the inaccuracies of the atomic data. However, the resultant stellar parameters were offset from previous determinations in the literature. We then modified the oscillator strengths and the van der Wals constants of our spectral regions to the values of Flores et al. (2019), which improved the stellar parameter determinations and the consistency with the literature. We used the Flores et al. (2019) modifications because they were obtained from spectra with a

spectral resolution close to IGRINS and for the same spectral regions we have employed.

Comparison with the literature: the bright YSOs in this work are canonical members of the Taurus-Auriga star-forming region and have numerous published parameters. Many of the prior works in the literature (e.g., Johns-Krull 2007; Pecaut & Mamajek 2013; Herczeg & Hillenbrand 2014) fixed parameters that we have left as variables in the fits. Prior studies also analyzed shorter wavelength regions of the YSO spectra, which are dominated by the hotter photosphere. Additionally, the variable nature of YSOs means that observations made at different epochs likely have different physical properties. In comparing our results to the literature, we find that the observed spectra and methods of Flores et al. (2019) provide the most direct comparisons and consistency.

5. Summary and Conclusions

We employed four different spectral regions of the infrared K band and an iterative MCMC approach to determine $T_{\rm eff}$, log g, B, and $v \sin i$ for a sample of canonical YSOs in the Taurus-Auriga star-forming region. Our analyses used a solar metallicity synthetic spectral grid of MARCS atmosphere models and the spectral synthesis code MOOGSTOKES. Our observational data were obtained with IGRINS.

We were able to reliably determine $T_{\rm eff}$, log g, and $v \sin i$ for 110 YSOs. Our ability to determine B is dependent on the $v \sin i$ and limited by the spectral resolution of IGRINS. We established that B values >1 kG or $(v \sin i/8)$ kG are required to provide meaningful B-field detections and that SNR > 150 is desirable for overall parameter fitting. Measurable B fields were found for 41 of the YSOs and upper limits were identified for the remaining objects.

The $T_{\rm eff}$ we derived agrees with previous temperature scales for spectral-type M YSOs, but it is systematically cooler for K stars. This could be a result of the models used in this analysis compared to others or the wavelength regions studied, which are more sensitive to the cool spotted regions of hotter YSOs. Our results show that the Class II and Class III objects are statistically similar in terms of $T_{\rm eff}$, marginally similar in $v \sin i$ and B, and different in log g and $r_{\rm K}$. The differences found in the distributions of log g and $r_{\rm K}$ correspond to the expected behavior of Class III being more evolved than Class II objects. We found mean log g values of 3.83 ± 0.03, 4.06 ± 0.04, and 4.22 ± 0.03 dex for the Taurus Class II and Class III objects and 19 TWA members, respectively. These differences are statistically significant and affirm the age gradient between these young star populations.

ORCID iDs

Ricardo López-Valdivia ⦿ https://orcid.org/0000-0002-7795-0018
Kimberly R. Sokal ⦿ https://orcid.org/0000-0002-3621-1155
Gregory N. Mace ⦿ https://orcid.org/0000-0001-7875-6391
Benjamin T. Kidder ⦿ https://orcid.org/0000-0002-2480-8552
Maryam Hussaini ⦿ https://orcid.org/0000-0001-9580-1043
Larissa Nofi ⦿ https://orcid.org/0000-0002-2387-5921
L. Prato ⦿ https://orcid.org/0000-0001-7998-226X
Christopher M. Johns-Krull ⦿ https://orcid.org/0000-0002-8828-6386
Heeyoung Oh ⦿ https://orcid.org/0000-0002-0418-5335
Jae-Joon Lee ⦿ https://orcid.org/0000-0003-0894-7824
Chan Park ⦿ https://orcid.org/0000-0002-2692-7520
Adam Kraus ⦿ https://orcid.org/0000-0001-9811-568X
Kyle F. Kaplan ⦿ https://orcid.org/0000-0001-6909-3856
Joe Llama ⦿ https://orcid.org/0000-0003-4450-0368
Andrew W. Mann ⦿ https://orcid.org/0000-0003-3654-1602
Hwihyun Kim ⦿ https://orcid.org/0000-0003-4770-688X
Michael A. Gully-Santiago ⦿ https://orcid.org/0000-0002-4020-3457
Soojong Pak ⦿ https://orcid.org/0000-0002-2548-238X
Narae Hwang ⦿ https://orcid.org/0000-0002-2013-1273
Daniel T. Jaffe ⦿ https://orcid.org/0000-0003-3577-3540

References

Adams, F. C., Lada, C. J., & Shu, F. H. 1987, ApJ, 312, 788
ALMA Partnership, Brogan, C. L., Pérez, L. M., et al. 2015, ApJL, 808, L3
Andre, P., Ward-Thompson, D., & Barsony, M. 1993, ApJ, 406, 122
Astropy Collaboration, Robitaille, T. P., Tollerud, E. J., et al. 2013, A&A, 558, A33
Astropy Collaboration, Price-Whelan, A. M., Sipőcz, B. M., et al. 2018, AJ, 156, 123
Attridge, J. M., & Herbst, W. 1992, ApJL, 398, L61
Baraffe, I., Homeier, D., Allard, F., & Chabrier, G. 2015, A&A, 577, A42
Barenfeld, S. A., Carpenter, J. M., Sargent, A. I., Isella, A., & Ricci, L. 2017, ApJ, 851, 85
Baruteau, C., Crida, A., Paardekooper, S. J., et al. 2014, in Protostars and Planets VI, ed. H. Beuther et al. (Tucson, AZ: Univ. Arizona Press), 667
Basri, G., & Batalha, C. 1990, ApJ, 363, 654
Basri, G., & Bertout, C. 1989, ApJ, 341, 340
Bean, J. L., Sneden, C., Hauschildt, P. H., Johns-Krull, C. M., & Benedict, G. F. 2006, ApJ, 652, 1604
Boccaletti, A., Di Folco, E., Pantin, E., et al. 2020, A&A, 637, L5
Bouvier, J., Matt, S. P., Mohanty, S., et al. 2014, in in Protostars and Planets VI, ed. H. Beuther et al. (Tucson, AZ: Univ. Arizona Press), 433
Bouvier, J., Tessier, E., & Cabrit, S. 1992, A&A, 261, 451
Calvet, N., Basri, G., & Kuhi, L. V. 1984, ApJ, 277, 725
Camenzind, M. 1990, RvMA, 3, 234
Casagrande, L., Flynn, C., & Bessell, M. 2008, MNRAS, 389, 585
Cieza, L. A., Kessler-Silacci, J. E., Jaffe, D. T., Harvey, P. M., & Evans, Neal J., I. 2005, ApJ, 635, 422
Correia, S., Zinnecker, H., Ratzka, T., & Sterzik, M. F. 2006, A&A, 459, 909
Cottaar, M., Covey, K. R., Meyer, M. R., et al. 2014, ApJ, 794, 125
Crockett, C. J., Mahmud, N. I., Prato, L., et al. 2012, ApJ, 761, 164
Cutri, R. M., Skrutskie, M. F., van Dyk, S., et al. 2003, yCat, 2246, 0
Deen, C. P. 2013, AJ, 146, 51
Doppmann, G. W., Jaffe, D. T., & White, R. J. 2003, AJ, 126, 3043
D'Orazi, V., Biazzo, K., & Randich, S. 2011, A&A, 526, A103
Duchêne, G., Monin, J. L., Bouvier, J., & Ménard, F. 1999, A&A, 351, 954
Ducourant, C., Teixeira, R., Galli, P. A. B., et al. 2014, A&A, 563, A121
Dyck, H. M., Simon, T., & Zuckerman, B. 1982, ApJL, 255, L103
Esplin, T. L., Luhman, K. L., & Mamajek, E. E. 2014, ApJ, 784, 126
Fischer, W., Edwards, S., Hillenbrand, L., & Kwan, J. 2011, ApJ, 730, 73
Flores, C., Connelley, M. S., Reipurth, B., & Boogert, A. 2019, ApJ, 882, 75
Flores, C., Reipurth, B., & Connelley, M. S. 2020, ApJ, 898, 109
Foreman-Mackey, D., Hogg, D. W., Lang, D., & Goodman, J. 2013, PASP, 125, 306
Gahm, G. F., Walter, F. M., Stempels, H. C., Petrov, P. P., & Herczeg, G. J. 2008, A&A, 482, L35
Gaia Collaboration, Brown, A. G. A., Vallenari, A., et al. 2018, A&A, 616, A1
Galli, P. A. B., Bertout, C., Teixeira, R., & Ducourant, C. 2015, A&A, 580, A26
Galli, P. A. B., Loinard, L., Ortiz-Léon, G. N., et al. 2018, ApJ, 859, 33
Gennaro, M., Prada Moroni, P. G., & Tognelli, E. 2012, MNRAS, 420, 986
Ghez, A. M., Neugebauer, G., & Matthews, K. 1993, AJ, 106, 2005
Ginsburg, A., Sipőcz, B. M., Brasseur, C. E., et al. 2019, AJ, 157, 98
Gray, D. F. 2005, The Observation and Analysis of Stellar Photospheres (3rd; Cambridge: Cambridge Univ. Press)
Greene, T. P., Wilking, B. A., Andre, P., Young, E. T., & Lada, C. J. 1994, ApJ, 434, 614
Gully-Santiago, M., Wang, W., Deen, C., et al. 2010, Proc. SPIE, 7739, 77393S
Gully-Santiago, M. A., Herczeg, G. J., Czekala, I., et al. 2017, ApJ, 836, 200
Gustafsson, B., Edvardsson, B., Eriksson, K., et al. 2008, A&A, 486, 951
Haas, M., Leinert, C., & Zinnecker, H. 1990, A&A, 230, L1
Haisch, Karl E., J., Lada, E. A., & Lada, C. J. 2001, ApJL, 553, L153
Harris, C. R., Millman, K. J., van der Walt, S. J., et al. 2020, Natur, 585, 357
Hartigan, P., Hartmann, L., Kenyon, S., Hewett, R., & Stauffer, J. 1989, ApJS, 70, 899
Hartmann, L., Hewett, R., Stahler, S., & Mathieu, R. D. 1986, ApJ, 309, 275
Hartmann, L. W., & Kenyon, S. J. 1990, ApJ, 349, 190
Hayashi, C. 1961, PASJ, 13, 450
Herbig, G. H. 1962, AdA&A, 1, 47
Herbig, G. H., & Bell, K. R. 1988, in Third Catalog of Emission-Line Stars of the Orion Population, Vol. 3 (Santa Cruz, CA: Lick Observatory), 90
Herbst, W., Eislöffel, J., Mundt, R., & Scholz, A. 2007, in in Protostars and Planets V, ed. B. Reipurth, D. Jewitt, & K. Keil (Tucson, AZ: Univ. Arizona Press), 297
Herczeg, G. J., & Hillenbrand, L. A. 2014, ApJ, 786, 97
Herczeg, G. J., & Hillenbrand, L. A. 2015, ApJ, 808, 23
Hernández, J., Calvet, N., Briceño, C., et al. 2007, ApJ, 671, 1784
Huang, J., Andrews, S. M., Cleeves, L. I., et al. 2018, ApJ, 852, 122
Hunter, J. D. 2007, CSE, 9, 90
Hussaini, M., Mace, G. N., López-Valdivia, R., Honaker, E. J., & Han, E. 2020, RNAAS, 4, 241
Ireland, M. J., & Kraus, A. L. 2008, ApJL, 678, L59
Jaffe, D. T., Keller, L. D., & Ershov, O. A. 1998, Proc. SPIE, 3354, 201
Johns-Krull, C. M. 2007, ApJ, 664, 975
Johns-Krull, C. M., & Valenti, J. A. 2001, ApJ, 561, 1060
Johns-Krull, C. M., Valenti, J. A., & Koresko, C. 1999, ApJ, 516, 900
Joy, A. H. 1949, ApJ, 110, 424
Kastner, J. H., Zuckerman, B., Weintraub, D. A., & Forveille, T. 1997, Sci, 277, 67
Kenyon, S. J., Gomez, M., Marzke, R. O., & Hartmann, L. 1994, AJ, 108, 251
Kenyon, S. J., & Hartmann, L. 1987, ApJ, 323, 714
Kenyon, S. J., & Hartmann, L. 1995, ApJS, 101, 117

Koenigl, A. 1991, ApJL, 370, L39
Konopacky, Q. M., Ghez, A. M., Rice, E. L., & Duchêne, G. 2007, ApJ, 663, 394
Kraus, A. L., Herczeg, G. J., Rizzuto, A. C., et al. 2017, ApJ, 838, 150
Kraus, A. L., & Hillenbrand, L. A. 2009, ApJ, 704, 531
Kraus, A. L., Ireland, M. J., Martinache, F., & Hillenbrand, L. A. 2011, ApJ, 731, 8
Kraus, A. L., White, R. J., & Hillenbrand, L. A. 2006, ApJ, 649, 306
Krolikowski, D. M., Kraus, A. L., & Rizzuto, A. C. 2021, AJ, 162, 110
Lada, C. J., Muench, A. A., Luhman, K. L., et al. 2006, AJ, 131, 1574
Langer, N., & Kudritzki, R. P. 2014, A&A, 564, A52
Lavail, A., Kochukhov, O., & Hussain, G. A. J. 2019, A&A, 630, A99
Lavail, A., Kochukhov, O., Hussain, G. A. J., et al. 2017, A&A, 608, A77
Lee, J.-J., Gullikson, K., & Kaplan, K. 2017, Igrins/Plp 2.2.0, Zenodo, doi:10.5281/zenodo.845059
Leinert, C., Haas, M., Mundt, R., Richichi, A., & Zinnecker, H. 1991, A&A, 250, 407
Leinert, C., Zinnecker, H., Weitzel, N., et al. 1993, A&A, 278, 129
Long, F., Herczeg, G. J., Harsono, D., et al. 2019, ApJ, 882, 49
López-Santiago, J., Crespo-Chacón, I., Flaccomio, E., et al. 2016, A&A, 590, A7
López-Valdivia, R. 2021a, Reduced IGRINS Spectra: Taurus-Auriga, V1, Harvard Dataverse, https://doi.org/10.7910/DVN/F9N2E0
López-Valdivia, R. 2021b, Reduced IGRINS spectra: TW Hydrae Association, V1, Harvard Dataverse, https://doi.org/10.7910/DVN/BHSMT6
López-Valdivia, R. 2021c, Codes and tools for IGRINS data: Synthetic grid, V1, Harvard Dataverse, https://doi.org/10.7910/DVN/ALOPIS
López-Valdivia, R., Mace, G. N., Sokal, K. R., et al. 2019, ApJ, 879, 105
Luhman, K. L. 1999, ApJ, 525, 466
Luhman, K. L. 2018, AJ, 156, 271
Luhman, K. L., Allen, P. R., Espaillat, C., Hartmann, L., & Calvet, N. 2010, ApJS, 186, 111
Luhman, K. L., Briceño, C., Stauffer, J. R., et al. 2003a, ApJ, 590, 348
Luhman, K. L., Mamajek, E. E., Shukla, S. J., & Loutrel, N. P. 2017, AJ, 153, 46
Luhman, K. L., Stauffer, J. R., Muench, A. A., et al. 2003b, ApJ, 593, 1093
Mace, G., Kim, H., Jaffe, D. T., et al. 2016, Proc. SPIE, 9908, 99080C
Mace, G., Sokal, K., Lee, J.-J., et al. 2018, Proc. SPIE, 10702, 107020Q
Mamajek, E. E. 2009, in AIP Conf. Ser., 1158, Exoplanets and Disks: Their Formation and Diversity, 1158, ed. T. Usuda, M. Tamura, & M. Ishii (Melville, NY: AIP), 3
Mann, A. W., Feiden, G. A., Gaidos, E., Boyajian, T., & von Braun, K. 2015, ApJ, 804, 64
Mann, A. W., Gaidos, E., & Ansdell, M. 2013, ApJ, 779, 188
Mathieu, R. D., Adams, F. C., & Latham, D. W. 1991, AJ, 101, 2184
Mathieu, R. D., Martin, E. L., & Magazzu, A. 1996, AAS Meeting, 188, 60.05
Muzerolle, J., Calvet, N., Hartmann, L., & D'Alessio, P. 2003, ApJL, 597, L149
Natta, A., Prusti, T., Neri, R., et al. 2001, A&A, 371, 186
Newton, E. R., Charbonneau, D., Irwin, J., & Mann, A. W. 2015, ApJ, 800, 85
Nguyen, D. C., Brandeker, A., van Kerkwijk, M. H., & Jayawardhana, R. 2012, ApJ, 745, 119

Nguyen, D. C., Jayawardhana, R., van Kerkwijk, M. H., et al. 2009, ApJ, 695, 1648
Nofi, L. A., Johns-Krull, C. M., López-Valdivia, R., et al. 2021, ApJ, 911, 138
Padgett, D. L. 1996, ApJ, 471, 847
Park, C., Jaffe, D. T., Yuk, I.-S., et al. 2014, Proc. SPIE, 9147, 91471D
Pecaut, M. J., & Mamajek, E. E. 2013, ApJS, 208, 9
Pérez, S., Casassus, S., Hales, A., et al. 2020, ApJL, 889, L24
Rajpurohit, A. S., Allard, F., Rajpurohit, S., et al. 2018, A&A, 620, A180
Rajpurohit, A. S., Reylé, C., Allard, F., et al. 2013, A&A, 556, A15
Rayner, J., Tokunaga, A., Jaffe, D., et al. 2016, Proc. SPIE, 9908, 990884
Reback, J., Jbrockmendel, & McKinney, W. 2021, pandas-dev/pandas: Pandas 1.3.4, Zenodo, doi:10.5281/zenodo.3509134
Rebull, L. M., Padgett, D. L., McCabe, C.-E., et al. 2010, ApJS, 186, 259
Reid, I. N., & Hawley, S. L. 2005, New Light on Dark Stars Red Dwarfs, Low-Mass Stars, Brown Stars (Berlin: Springer)
Ribas, Á., Bouy, H., & Merín, B. 2015, A&A, 576, A52
Ribas, Á., Merín, B., Bouy, H., & Maud, L. T. 2014, A&A, 561, A54
Richichi, A., Ragland, S., Calamai, G., et al. 1999, A&A, 350, 491
Riedel, A. R., Finch, C. T., Henry, T. J., et al. 2014, AJ, 147, 85
Ruíz-Rodríguez, D., Ireland, M., Cieza, L., & Kraus, A. 2016, MNRAS, 463, 3829
Ryabchikova, T., Piskunov, N., Kurucz, R. L., et al. 2015, PhyS, 90, 054005
Santos, N. C., Melo, C., James, D. J., et al. 2008, A&A, 480, 889
Schaefer, G. H., Prato, L., Simon, M., & Patience, J. 2014, AJ, 147, 157
Schmidt-Kaler, T. 1982, in in Landolt-Börnstein—Group VI Astronomy and Astrophysics, ed. K. Schaifers & H. H. Voigt (Berlin: Springer)
Simon, M., Chen, W. P., Howell, R. R., Benson, J. A., & Slowik, D. 1992, ApJ, 384, 212
Simon, M., Guilloteau, S., Beck, T. L., et al. 2019, ApJ, 884, 42
Sneden, C. A. 1973, PhD thesis, Univ. Texas Austin
Soderblom, D. R., Pendleton, J., & Pallavicini, R. 1989, AJ, 97, 539
Sokal, K. R., Deen, C. P., Mace, G. N., et al. 2018, ApJ, 853, 120
Sokal, K. R., Johns-Krull, C. M., Mace, G. N., et al. 2020, ApJ, 888, 116
Straižys, V. 1992, Multicolor Stellar Photometry (Tucson, AZ: Pachart Publishing House)
Valenti, J. A., Basri, G., & Johns, C. M. 1993, AJ, 106, 2024
Varga, J., Gabányi, K. É., Ábrahám, P., et al. 2017, A&A, 604, A84
Virtanen, P., Gommers, R., Oliphant, T. E., et al. 2020, NatMe, 17, 261
Walter, F. M., Brown, A., Mathieu, R. D., Myers, P. C., & Vrba, F. J. 1988, AJ, 96, 297
Wang, W., Gully-Santiago, M., Deen, C., Mar, D. J., & Jaffe, D. T. 2010, Proc. SPIE, 7739, 77394L
Webb, R. A., Zuckerman, B., Platais, I., et al. 1999, ApJL, 512, L63
Weintraub, D. A. 1989, PhD thesis, Univ. California, Los Angeles
Wright, J. T., & Eastman, J. D. 2014, PASP, 126, 838
Yang, H., & Johns-Krull, C. M. 2011, ApJ, 729, 83
Yang, H., Johns-Krull, C. M., & Valenti, J. A. 2005, ApJ, 635, 466
Yao, Y., Meyer, M. R., Covey, K. R., Tan, J. C., & Da Rio, N. 2018, ApJ, 869, 72
Yuk, I.-S., Jaffe, D. T., Barnes, S., et al. 2010, Proc. SPIE, 7735, 77351M
Zuckerman, B., & Song, I. 2004, ARA&A, 42, 685